

A novel passive flow control technique using circular arcs coupled with downstream splitters

Eydi, Faezeh; Mojra, Afsaneh; Hooman, Kamel

DOI

[10.1016/j.oceaneng.2024.119393](https://doi.org/10.1016/j.oceaneng.2024.119393)

Publication date

2024

Document Version

Final published version

Published in

Ocean Engineering

Citation (APA)

Eydi, F., Mojra, A., & Hooman, K. (2024). A novel passive flow control technique using circular arcs coupled with downstream splitters. *Ocean Engineering*, 313, Article 119393.
<https://doi.org/10.1016/j.oceaneng.2024.119393>

Important note

To cite this publication, please use the final published version (if applicable).
Please check the document version above.

Copyright

Other than for strictly personal use, it is not permitted to download, forward or distribute the text or part of it, without the consent of the author(s) and/or copyright holder(s), unless the work is under an open content license such as Creative Commons.

Takedown policy

Please contact us and provide details if you believe this document breaches copyrights.
We will remove access to the work immediately and investigate your claim.

Green Open Access added to TU Delft Institutional Repository

'You share, we take care!' - Taverne project

<https://www.openaccess.nl/en/you-share-we-take-care>

Otherwise as indicated in the copyright section: the publisher is the copyright holder of this work and the author uses the Dutch legislation to make this work public.



Research paper

A novel passive flow control technique using circular arcs coupled with downstream splitters

Faezeh Eydi^a, Afsaneh Mojra^{a,*}, Hooman Kamel^{b,**}

^a Department of Mechanical Engineering, K. N. Toosi University of Technology, Iran

^b Department of Mechanical Engineering, Delft University of Technology, Netherlands

ARTICLE INFO

Keywords:

Vortex-induced vibration
Circular cylinder
Passive control
Arc plates
Splitter plates
Energy harvesting

ABSTRACT

The current study presents a novel piezoelectric design that converts vortex-induced vibrations caused by flow across a circular cylinder. This design can be implemented as a passive control method for energy harvesting. It encompasses the novelty of employing circular arc plates around a circular cylinder integrated with flexible splitters downstream. To assess the merits of the proposed design, a comprehensive parametric study for flexible splitters is conducted to specify the optimum layout of piezoelectric harvesters. The analysis is carried out at a low Reynolds number, $Re = 100$, at which accurate non-intrusive experimental assessment of flow structure is difficult. The results indicate that the drag can be halved by adding circular arc plates to the cylinder. Moreover, it is demonstrated that the plate displacement increases by 18.29 folds for dual splitters compared with a single plate. By adding the arc plates, a further increase of 3.97 folds is obtained. Following this, the maximum strain with the inclusion of arc plates is 170.17% higher than the cylinder without arc plates (bare cylinder) for dual flexible splitters downstream, enhancing the energy harvesting performance remarkably. Finally, using the proposed design, the generated electrical power figures out at $3.13 \mu W$ at 77.7% conversion efficiency.

Abbreviations

ALE	Arbitrary Lagrangian-Eulerian	U^*	Non-dimensional mean streamwise velocity
FFT	Fast Fourier transform	X/Y	Reference coordinates in material frame
FSI	Fluid-structure interaction	x/y	Spatial coordinates in spatial frame
CAP	Cylinder with arc plates	F	Deformation gradient tensor
PEH	Piezoelectric harvester	R	External electrical load resistance [Ω]
RMS	Root-mean-square	t	Time [s]
VIV	Vortex-induced vibration	C	Fourth-order elasticity tensor
MEMS	Micro-electro-mechanical systems	Re	Reynolds number
WSNs	Wireless sensor networks	u_s	Displacement vector [m]
BDF	Backward differential formula	A	Tip amplitude of splitter plates [m]
CFL	Courant–Friedrichs–Lewy	A^*	Non-dimensional form of tip amplitude
PTC	Passive turbulence control	I	Unit diagonal matrix

(continued on next column)

(continued)

Nomenclature		f	Force in the spatial frame [N]
C_{lms}	RMS of lift coefficient	F	Force in the material frame [N]
$\overline{C_p}$	Time-averaged pressure coefficient	dv	Scale factor for the material frame
$\overline{C_{pb}}$	Time-averaged base pressure coefficient	u_f	Fluid velocity [m/s]
$\overline{C_d}$	Time-averaged drag coefficient	u_m	Fluid velocity in moving coordinates [m/s]
D_{SV}	Horizontal distance between two successive vortices [m]	v_s	Velocity of splitter plate [m/s]
St	Strouhal number	E_{el}	Electric field [v]
d	Cylinder diameter [m]	V	Electric potential [v]
\hat{d}	Diameter of arc plates [m]	e	Piezoelectric coupling tensor
D	Electric displacement [C/m^2]	k_0	Vacuum permittivity [F/m]
L	Length of splitter plate [m]	K	Second-order tensor of dielectric
p	Fluid pressure [Pa]	Greek symbols	

(continued on next page)

* Corresponding author.

** Corresponding author.

E-mail addresses: mojra@kntu.ac.ir (A. Mojra), k.hooman@tudelft.nl (H. Kamel).

<https://doi.org/10.1016/j.oceaneng.2024.119393>

Received 26 June 2024; Received in revised form 30 August 2024; Accepted 18 September 2024

Available online 30 September 2024

0029-8018/© 2024 Elsevier Ltd. All rights reserved, including those for text and data mining, AI training, and similar technologies.

(continued)

P	Distance between splitter plates [m]	ϵ	Green–Lagrange strain
P^*	Non-dimensional splitters' distance	ϵ_{max}	Maximum strain of splitter plates
S	Cylinder–first splitter distance [m]	η	Power conversion factor [W]
S^*	Non-dimensional form of S	θ	Angle of cylinder surface
u^*	Non-dimensional RMS of streamwise velocity	α	Coverage angle of arc plates
v^*	Non-dimensional RMS of transverse velocity	σ	Cauchy stress [Pa]
P_{rms}	RMS of static pressure [Pa]	Γ	Stress tensor of fluid [Pa]
W_z^*	Non-dimensional spanwise vorticity	μ	Dynamic viscosity [Pa.s]
U_∞	Freestream velocity [m/s]	ρ	Fluid density [kg/m ³]

1. Introduction

With the growing application of microtechnologies, microelectronic devices including actuators, health monitors, medical implants, and biosensors attract more attention (Xiong and Wang, 2016). Therefore, the demand for low-power electronic devices such as

micro-electro-mechanical-systems (MEMS) and wireless sensor networks (WSNs) (Benedetti et al., 2019; Stamatellou and Kalfas, 2019; Zhao et al., 2019) is on the rise. However, the main power source for these devices is batteries with limited operational life and rather high decommissioning costs as chemical waste (Rezaei et al., 2022). A sustainable and environmentally-friendly alternative is to convert vibrational energy to electricity on the spot through small-scale micro-power plants; for instance, using piezoelectrics. Piezoelectric polymers are simple structures that generate power at high voltage (Abdelkefi, 2016). Similarly, electricity generation through transverse galloping (Xu et al., 2021; Yu and Zhang, 2021), vortex-induced vibration (VIV) (Asok et al., 2024; Lai et al., 2021; Su and Lin, 2020; Wang et al., 2021b), flutter (Caracoglia, 2018; Zhang et al., 2020), and a combination of these techniques (Qin et al., 2019; Yu et al., 2019) have been investigated in the literature. For instance, circular cylinders in cross-flow are known to cause vortex-induced vibration (Amini and Zahed, 2024). The VIV provides high amplitude vibration, but its application is limited to a narrow range of wind speeds within which the lock-in or synchronization phenomenon happens. Also, the frequency of vortex shedding

Table 1
Literature review on wake control and energy harvesting from various cross sections.

Authors	Study	Exp./ Num.	Cross section	Re	Finding	Wake control	Energy harvesting
Durhasan (Durhasan, 2020)	Investigation of hollow square cylinder with five different slot ratios	Exp.	Square	6000	The most drag reduction of 42% at slot ratio of 0.05	☑	☒
Eydi et al. (Eydi et al., 2022)	Effect of detached flexible and rigid splitter plates in the form of single and dual plates.	Num.	Circle	100	Significant effect of doubling number of splitter plates on the performance of wake control and energy harvesting	☑	☑
Chauhan et al. (Chauhan et al., 2019)	Wake control using control rods	Exp.	Square	485, 805, 1290	22% decrease in drag coefficient	☑	☒
Binyet et al. (Binyet et al., 2020)	Piezoelectric energy harvesting using flexible plate	Exp.	Square	9200–14300	Lower conversion efficiency in spite of great power output in long plates	☒	☑
Mashhadi et al. (Mashhadi et al., 2021)	Effect of Re and aspect ratio (AR) of a rectangular cylinder	Num.	Rectangle	30–200	Increase of vortex strength with Re and decrease with AR	☑	☒
Zhang et al. (Zhang et al., 2021)	Effect of Re on piezoelectric energy harvesting from VIV	Exp.	Circle	500–3300	More sensitivity to Re at low damping ratio	☑	☑
Sun et al. (Sun et al., 2021)	Investigation of VIV response of flexible plate	Num.	Square	100	Significant impact of bending rigidity and plate length on VIV	☑	☒
Ozkan et al. (Ozkan et al., 2017)	Effect of permeable and inclined short plates on vortex shedding suppression	Exp.	Circle	5×10^3	Significant drag reduction of 74% for porosity of 0.4 and plate angle of 45°	☑	☒
Assi et al. (Assi et al., 2019)	Wake suppression by eight controlled rotating cylinders	Num.	Circle	100	Decrease of overall drag coefficient with increase of rotation speed	☑	☒
Zhu and Liu (Zhu and Liu, 2020)	Effect of length and surface undulation of rigid wavy plate on vortex shedding	Num.	Circle	150	27.5% and 54.9% decrease in mean drag and lift fluctuations	☑	☒
Sharma and Dutta (Sharma and Dutta, 2020)	Influence of rigid and flexible splitters at different ratios of L/B (B: blocking width of cylinder, L: length of splitters)	Exp.	Square	600,1000, 2000	Maximum reduction of Strouhal number (77.31% and 79.41%) at L/B = 8 in cases of rigid (Re = 1000) and flexible (Re = 2000) plates	☑	☒
Taheri et al. (Taheri et al., 2021)	Mass ratio and the Keulegan-Carpenter number effects on output power from oscillatory flow	Num.	Circle	150	Independence of the best power from mass ratio and its reduction with Keulegan-Carpenter number	☒	☑
Chehreh and Javadi (Chehreh and Javadi, 2018)	Effect of two attached plates at ±55° on back of cylinder, oscillating at different ratios of the natural frequency	Num.	Circle	100, 200	Observation and classification of different flow patterns	☑	☒
Nam and Yoon (Nam and Yoon, 2022)	Flow control with the help of wavy geometry at different aspect ratios	Num.	Ellipse	100	Observation of three modes in bifurcation: steady, unsteady and coexistent	☑	☒
Zhu et al. (Zhu et al., 2020)	Study of flow induced vibration using upstream and downstream splitters that placed individually and simultaneously	Num.	Circle	120	Elimination or excitation of galloping at different arrangements of splitters	☑	☒
Eydi and Mojra (Eydi and Mojra, 2023)	Investigation of using two arc plates for flow and noise control	Num.	Circle	22×10^3	Significant drag reduction of 39% by inclusion of arc plates	☑	☒
Wang et al. (Wang et al., 2021a)	Enhancing the effectiveness of energy harvesting system using downstream rectangular plate at different dimension and location	Exp.	Circle	$27 \times 10^3 - 189 \times 10^3$	The efficient plate is a 2D-high in the 0.2D~0.4D space of cylinder	☒	☑

approaches the natural frequency of the structure. Out of this range, high amplitude vibration occurs (Song et al., 2017). Accordingly, the performance of cylinder-based wind energy harvesters by VIV is restricted. Hence, numerous studies have been conducted on designing, improving, or developing wind energy harvesters. Hu et al. (2018) performed an experimental study on wind energy harvesting from the cylinder based on the VIV mechanism. They increased the harvester efficiency by three rods with different shapes of cross-sections such as circular, triangular, and square. It was found that the highest harvested energy belonged to the triangular one compared to other shapes of cross sections. Liu et al. (2020) amended the harvested wind energy using double upstream plates at different horizontal and vertical distances from the cylinder. Their results revealed that the plates changed the vibration amplitude from the VIV region to the galloping. Ding et al. (2015) studied the flow-induced vibrations and energy harvesting from a cylinder in a 2D unsteady RANS simulations with different shapes of cross-sections including circular sections with passive turbulence control (PTC), square, Q-trapezoid, and triangular sections. Based on their findings, the PTC and Q-trapezoid have greater flow-induced motions than other cross-sectional shapes, which resulted in enhanced energy harvesting with maximum efficiency of 37.9% and 45.7%, respectively. In the fully-developed galloping region, maximum energy harvesting from the PTC-cylinder and Q-trapezoid cross-sections were equal to 25.67W and 24.45W, respectively. Wang et al. (2019) improved the wind energy harvester's performance by attaching Y-shaped structures to the cylinder. It was found that the proposed structure performed better than a square, which is one of the most effective structures for galloping mechanisms. Kan et al. (2021), coupled the VIV and the galloping using a diamond-shaped baffle at the cylinder downstream to alter the aeroelastic instability and improve the harnessed vibrational wind energy.

Although vortex shedding leads to a significant amount of vibrational energy, it has a destructive effect on the circular structure due to the VIV (Duranay, 2024; Moradi and Mojra, 2024b; Zhu et al., 2017), which makes it crucial to control the wake formation using active and passive control methods. In active control, the flow is weakened using an external energy source. Examples are blowing and suction (Rastan et al., 2019; Xue et al., 2021), rotation (Karimi-Zindashti and Kurç, 2024), electromagnetic force (Jiang et al., 2022), and synthetic jet (Wang et al., 2016). However, passive control relies on modifying the surface or shape of the structure for instance slotted circular cylinder (Bao et al., 2018; Sharma and Barman, 2020), splitter plates (Eydi et al., 2022; Moreno et al., 2023), passive-jet flow control (Liu et al., 2024), arc plates (Eydi and Mojra, 2023), shape modification (Moradi and Mojra, 2024a; Yang et al., 2020), and surface bumps (Derakhshandeh and Gharib, 2021). Compared with active counterparts, passive control strategies do not need additional energy and are easier to implement with lower maintenance costs (Mishra et al., 2020). Table 1 provides an overview of recent studies based on wake control and energy harvesting of various cross sections.

A review of the literature shows that only a handful of studies investigate both wake control and energy conversion (see the last two columns in Table 1). Thus, in this work, besides control objectives, a high-efficiency cylinder-based harvester is designed with piezoelectric polymers.

This design includes arc plates around the cylinder with piezoelectric-attached-flexible splitters further downstream. The hypothesis is that while these two additional features, arc plates, and dual splitters, will lead to higher energy conversion efficiency, they will also lead to effective flow control. To optimize the proposed design, the plate-cylinder distance is parametrically varied to specify the optimum placement of the piezoelectric harvesters (PEHs). The analysis is carried out at $Re = 100$. At such low Re values, accurate experimental investigations are prohibitively difficult (Zhu and Zhou, 2019). In addition, three-dimensional flow inherece appears at Reynolds number above 160 (Mansy et al., 1994). Thus, manipulation of the

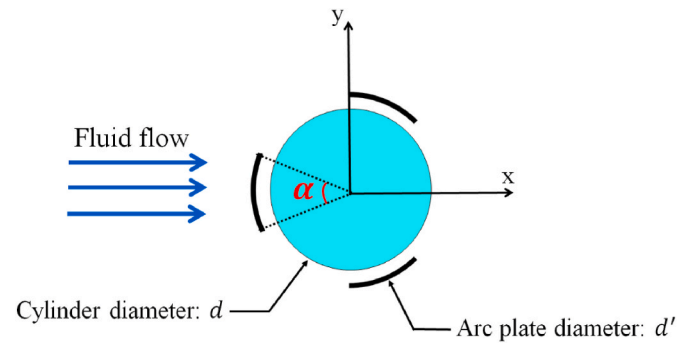


Fig. 1. Illustration of a cylinder with three arc plates (CAP): d is the cylinder diameter, d' is the diameter of arc plates, and α is the coverage angle of arc plates.

two-dimensional FSI (fluid-structure interaction) problem using ALE (arbitrary Lagrangian–Eulerian) method can provide reasonable results for this study.

There are four sections in the remainder of this work. Section 2 provides further details on numerical methods and the validation of the simulation model. The results of flow quantities and energy harvesting performance are discussed in Section 3, and eventually, Section 4 draws the conclusions.

2. Numerical method

2.1. Conceptual design of system

Considering the successful application of flexible splitter plates in flow control or energy fields (Naseer et al., 2017; Sun et al., 2019), this study explores the benefits of downstream flexible splitters accompanied by arc plates. To this end, three concentric arc plates are located around the cylinder symmetrically as presented in Fig. 1. One of them is placed in front of the cylinder to directly influence the front stagnation point of the cylinder by which the pressure drag significantly reduces and consequently the total drag reduces. The other two arc plates are placed at the top and bottom of the rear portions of the cylinder, affecting separation points, and ultimately influencing the flow structure. The coverage angle (α) and the diameter of arc plates (d') are equal to 45° and $1.2d$ (d is the cylinder diameter), respectively. As demonstrated in Fig. 2, for this study, two-cylinder cases are considered: (1) cylinder with arc plates which for the sake of convenience is called CAP in the rest of this study, and (2) bare cylinder. In addition, flexible splitters are placed downstream of these two-cylinder cases in the single and dual forms. The gap distances between cylinder-first plate and plate-plate are considered by parameters of S and P , respectively. The ratios of S and P to the cylinder diameter (d) are defined by S^* and P^* , which vary in the ranges of $0 \leq S^* \leq 2.5$ and $0 \leq P^* \leq 3$, respectively. Furthermore, the leading edge of all splitter plates is fixed. However, in the dual configuration of the CAP case, the trailing edge of the second plate is fixed to enhance the plate's oscillation for energy harvesting. In addition, a piezoelectric sheet with an external resistance of $1 \text{ k}\Omega$ is attached at the free tip of each splitter (two in total) as cantilever beams. The piezoelectric sheets are electrically insulated at their left and right edges. In all configurations, the length of splitters (L) are similar and set to cylinder diameter ($\frac{L}{d} = 1$). The thickness of all splitter plates is considered to be $0.03d$ (Abdi et al., 2017; Turek and Hron, 2006). Additionally, the thickness of arc plates and piezoelectric sheets are assumed $0.01d$, and $0.005d$, respectively. Such dimensions are chosen based on structural integrity requirements and empirical design practices commonly used in similar studies (Eydi and Mojra, 2023). The selected thicknesses aim to provide enough mechanical strength to withstand expected

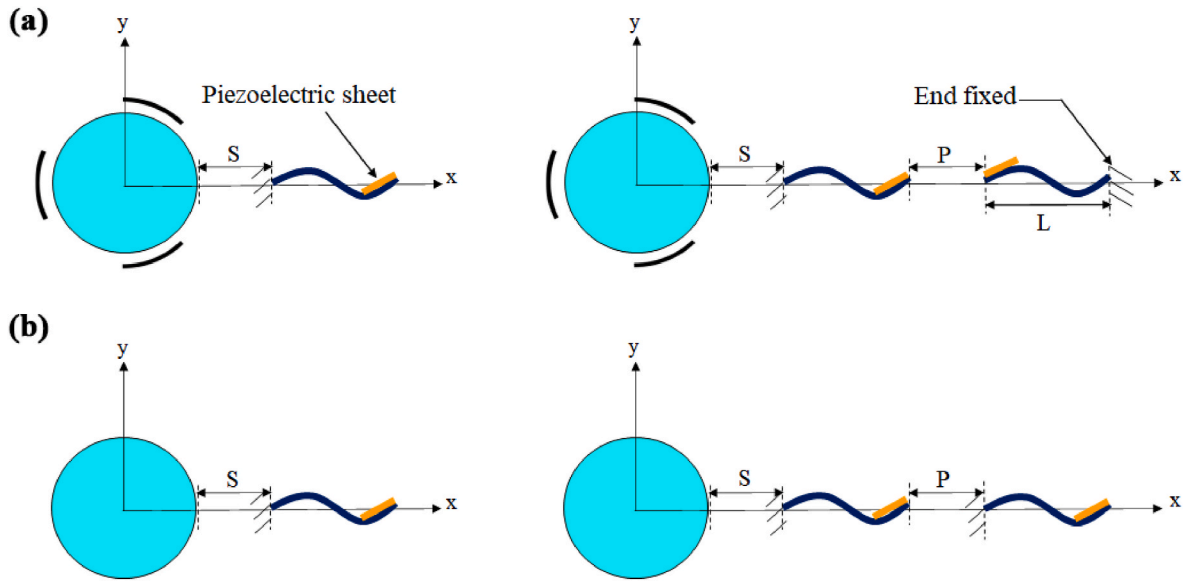


Fig. 2. Schematic of flexible splitter plates in the single and dual forms for: (a) CAP and (b) bare cylinder; L is the length of flexible splitter plates, and S and P are the cylinder-first plate and plate-plate gap spacings. The leading edge of all splitter plates is fixed except the second plate of CAP in which the trailing edge is fixed.

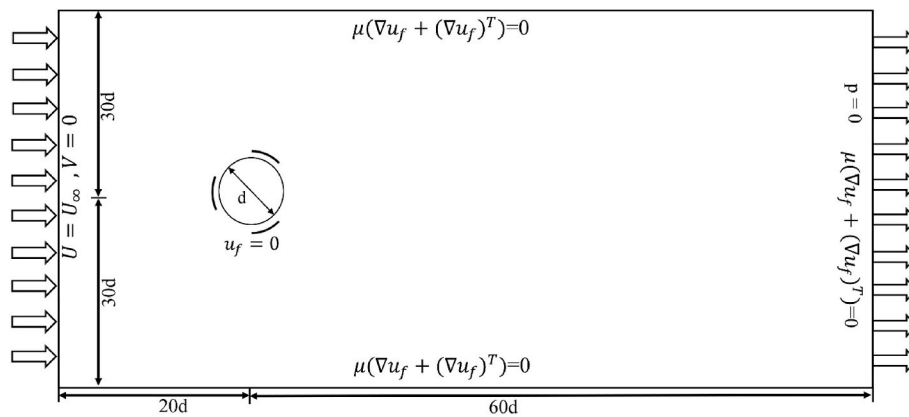


Fig. 3. Computational domain and the assigned boundary conditions.

hydrodynamic loads while minimizing unnecessary material usage that could affect flow dynamics negatively.

Fig. 3 shows an illustration of the computational domain and the assigned boundary conditions in the presence of the CAP in the origin. The size of the rectangular domain is $80d \times 60d$ which is sufficiently large in both flow and cross-flow directions (Abdi et al., 2019; Eydi et al., 2022). The two lateral borders are set $30d$ away from the cylinder center, while the cylinder center is located at the distance of $20d$ from the inlet. In this problem, the blockage ratio is found to be 1.66%, which is significantly lower than the threshold commonly accepted in the literature (typically less than 5%) for negligible blockage effects. Given this low blockage ratio, the influence of the domain boundaries on the flow field around the cylinder is minimal. Therefore, the results are unaffected by domain constraints and blockage effects.

Regarding the inlet boundary in Fig. 3, the U variable refers to the velocity component of the fluid in the horizontal direction (along the x -axis). In the present simulation, $U = U_\infty$ indicates a horizontal uniform inlet flow to the computational domain. The variable V represents the velocity component of the fluid in the vertical direction (along the y -axis). At the inlet $V = 0$, which means there is no vertical movement of the fluid as it enters the domain. At the outlet, the fluid flow exits without experiencing any pressure gradient ($p = 0$). Top and bottom domain boundaries expose the open boundary condition. The surface of

the cylinder and arc plates are subject to the no-slip boundary condition. In all simulations, the domain associated with the cylinder and the arc plates is modeled as a rigid body. However, the splitter plates are modeled using a flexible body approach that interacts with the fluid domain based on the principles of two-way fluid-structure interaction. With regards to this, a cylinder diameter of 0.1 m, a fluid density of $1260 \frac{kg}{m^3}$, a dynamic viscosity of $1.42 Pa.s$ and a flow velocity of $1.127 \frac{m}{s}$, which corresponds to $Re = 100$ are considered. The solid domain is characterized by material properties including a Young modulus of 32 MPa, a Poisson's ratio of 0.3, and a density of $180 \frac{kg}{m^3}$ (Eydi et al., 2022; Turek and Hron, 2006).

2.2. Governing equations

Fully coupled interaction between a flexible splitter and an incompressible fluid is studied using the ALE method which couples the fluid flow equations based on the Eulerian description with the equations of solid deformation based on the Lagrangian description (Averweg et al., 2024; Monteleone et al., 2022; Richter and Wick, 2010). Moreover, the moving mesh strategy is utilized which adjusts mesh refinement with the structural motion. The governing equations of fluid flow, solid mechanics, energy generation by piezoelectric sheets, coupling, and

moving mesh are discussed in the following.

2.2.1. Fluid dynamics

Mass continuity and Navier-Stokes equation for an incompressible Newtonian fluid flow in the spatial (deformed) coordinate system are (Díaz-Ojeda et al., 2019):

$$\nabla \cdot u_f = 0 \quad (1)$$

$$\rho \left(\frac{\partial u_f}{\partial t} + (u_f - u_m) \cdot \nabla u_f \right) = \nabla \cdot [-pI + \mu(\nabla u_f + (\nabla u_f)^T)] \quad (2)$$

where, ρ is the fluid density, u_f and u_m are the velocity vectors in fixed and moving coordinate systems, p is the pressure, I is the unit diagonal matrix, and μ is the dynamic viscosity. The initial conditions for solving fluid equations are $u_f = 0$ and $p = 0$. Moreover, as ALE uses different coordinate systems, a force transformation is also required:

$$F = f \cdot \left(\frac{dv}{dV} \right) \quad (3)$$

Here, f and F are the force in the spatial and the material frames, respectively, while the scale factors in two frames are denoted by dv and dV , respectively.

2.2.2. Solid mechanics

Based on the constitutive law, solid mechanics can be numerically formulated as follows:

$$(S_{PK2} - S_{PK2_0}) = C : (\varepsilon - \varepsilon_0) \quad (4)$$

Here, S_{PK2} is the second Piola–Kirchhoff stress tensor and C is the fourth-order elasticity tensor, ε is the Green–Lagrange strain, “:” is the double-dot tensor product (double contraction). S_{PK2_0} and ε_0 are the initial values. The Green–Lagrange strain (ε) is formulated as:

$$\varepsilon = 0.5 [(\nabla u_s)^T + \nabla u_s + (\nabla u_s)^T \nabla u_s] \quad (5)$$

Here, u_s denotes the displacement vector which is calculated by:

$$\rho_s \frac{\partial^2 u_s}{\partial t^2} - \nabla \cdot \sigma = F_V \quad (6)$$

where, ρ_s is the density and F_V is the force per unit volume at the fluid–solid interface, σ is the Cauchy stress which is related to the second Piola–Kirchhoff stress by $\sigma = J^{-1}FSF^T$, in which $F = I + \nabla u_s$ and is the deformation gradient tensor, and $J = \det(F)$ (Eydi et al., 2022). The initial conditions used to solve Eq. (6) are $u_s = 0$ and $\frac{\partial u_s}{\partial t} = 0$.

2.2.3. Piezoelectric sheet

The balance equation in piezoelectric material based on Gauss’s law is as follows:

$$\nabla \cdot D = 0 \quad (7)$$

Here, D is electric displacement, which is given by:

$$D = e\varepsilon + k_0KE_{el} \quad (8)$$

where, e is the piezoelectric coupling tensor, k_0 is the vacuum permittivity, K is the second-order tensor of dielectric relative permittivity measured at constant applied stress, and $E_{el} = -\nabla V$ is the electric field, in which V is the electric potential in the piezoelectric material (Curatolo et al.).

The average harvested power of piezoelectric (P) is obtained by:

$$P = \frac{V_{rms}^2}{R} \quad (9)$$

where, R is the resistance load and has a fixed value of $1 \text{ k}\Omega$ in the rest of this study and $1 \text{ k}\Omega_{rms}$ is the RMS of the output voltage. The output

voltage is computed through $E_{el} = -\nabla V$ in Eq. (8). Based on this, the power can be achieved.

Furthermore, to evaluate the efficiency of energy harvester system, power conversion factor (η) is calculated by:

$$\eta = \frac{P}{P_{fluid}} \quad (10)$$

where, P_{fluid} is the available fluid power, which is given by:

$$P_{fluid} = \frac{1}{2} \rho_{fluid} U_\infty^3 bL \quad (11)$$

Here, ρ_{fluid} is the fluid density, U_∞ is the flow velocity, and b and L are the flow ward width and length of the body.

2.2.4. Coupling and interface considerations

The following boundary condition is applied at the fluid–solid interface:

$$u_f = v_s \quad (12)$$

where, $v_s = \frac{\partial u_s}{\partial t}$ is the plate velocity. Additionally, the stress equilibrium at the interface of the two domains is calculated by:

$$\Gamma \cdot n^f + \sigma \cdot n^s = 0 \quad (13)$$

Here, n^f and n^s are the outward normal vectors, and Γ and σ are the stress tensors of fluid and solid structure, respectively. The addition of the pressure with the viscous stress yields the fluid tensor equation:

$$\Gamma = -pI + \mu(\nabla u_f + (\nabla u_f)^T) \quad (14)$$

For the contact interface of the piezoelectric and the structural solids, a null reference electrical potential ($V = 0$) is applied. Furthermore, an electric potential of $V = \tilde{V}$ is imposed on the top edge of the piezoelectric sheet, such that the following equation holds (Curatolo et al.):

$$\int \dot{D} \cdot n ds = \frac{\tilde{V}}{R} \quad (15)$$

Here, R denotes the external electrical load resistance.

2.2.5. Moving mesh

The computational mesh is deformed to adapt to the flexible plates’ deformations. By utilizing the Winslow smoothing method for the moving mesh, the deformation of the mesh domain is related to the original shape (Knupp, 1999). According to this method, the mesh matches the structure movement, and a new mesh is obtained for the fluid domain.

$$\frac{\partial^2 \partial X}{\partial x^2 \partial t} + \frac{\partial^2 \partial X}{\partial y^2 \partial t} = 0 \quad (16)$$

$$\frac{\partial^2 \partial Y}{\partial x^2 \partial t} + \frac{\partial^2 \partial Y}{\partial y^2 \partial t} = 0 \quad (17)$$

Here, X and Y stand for the reference coordinates in the material frame, and x and y are the coordinate system in the spatial frame.

2.3. Flow characteristics parameters

The flow parameters include the spanwise vorticity (W_z), the mean drag coefficient ($\overline{C_d}$), the lift coefficient (C_l), the Strouhal number (St), the time-averaged of pressure coefficient ($\overline{C_p}$), the time-averaged of base pressure coefficient ($\overline{C_{pb}}$), the RMS of streamwise and transverse velocities (u_{rms} and v_{rms}), the lift coefficient ($C_{l_{rms}}$), the static pressure (P_{rms}), and the time-averaged streamwise velocity (\overline{u}) are defined as follows:

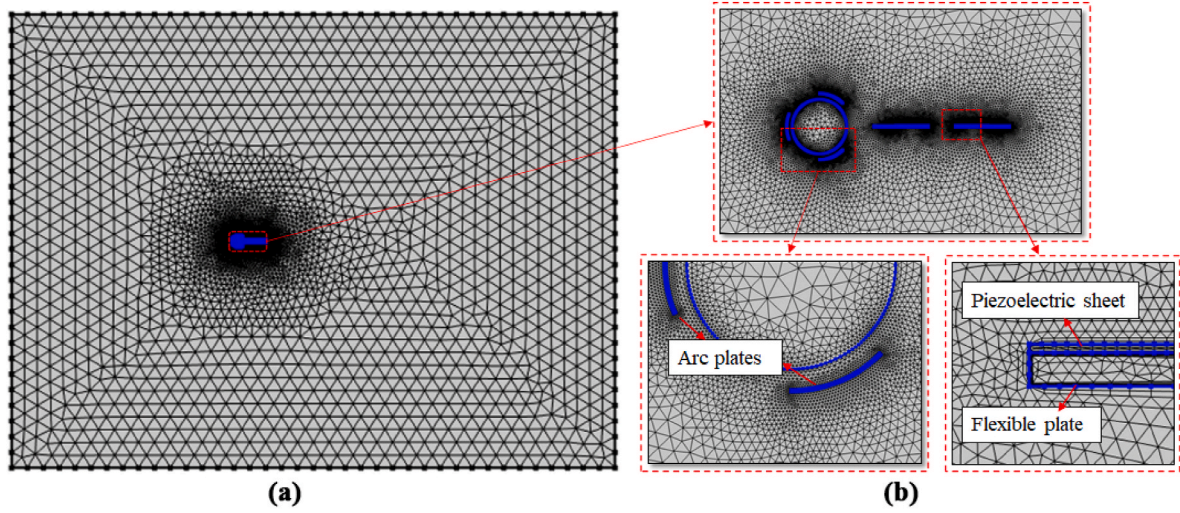


Fig. 4. Mesh structure of: (a) view of the entire domain, mesh refinement is performed close to the structure boundaries, (b) close view of the mesh around the arc plates, flexible plate, and piezoelectric sheet.

$$W_z = \frac{\partial v}{\partial x} - \frac{\partial u}{\partial y} \quad (18)$$

$$\overline{C_d} = \frac{1}{N} \sum_{i=1}^N \frac{F_d}{0.5\rho U_\infty^2 d} \quad (19)$$

$$C_l = \frac{F_l}{0.5\rho U_\infty^2 d} \quad (20)$$

$$St = \frac{f_s d}{U_\infty} \quad (21)$$

$$\overline{C_p} = \frac{1}{N} \sum_{i=1}^N \frac{P_i - P_\infty}{0.5\rho U_\infty^2} \quad (22)$$

$$\overline{C_{pb}} = \frac{1}{N} \sum_{i=1}^N \frac{P_{b_i} - P_\infty}{0.5\rho U_\infty^2} \quad (23)$$

$$u_{rms} = \sqrt{\frac{1}{N} \sum_{i=1}^N (u_i - \bar{u})^2} \quad (24)$$

$$v_{rms} = \sqrt{\frac{1}{N} \sum_{i=1}^N (v_i - \bar{v})^2} \quad (25)$$

$$P_{rms} = \sqrt{\frac{1}{N} \sum_{i=1}^N (P_i - \bar{P})^2} \quad (26)$$

$$C_{lms} = \sqrt{\frac{1}{N} \sum_{i=1}^N (C_{l_i} - \overline{C_l})^2} \quad (27)$$

$$\bar{u} = \frac{1}{N} \sum_{i=1}^N (u_i) \quad (28)$$

Here, f_s is the frequency of vortex shedding, F_d and F_l are the drag and lift forces, P , P_∞ and P_b denote the static pressure, reference pressure of the inlet and the pressure at the rear stagnation point, respectively. u and v are the velocities parallel and perpendicular to the flow, respectively. N is the number of samples in the time history, u_i , v_i , P_i and C_{l_i} are the temporal series.

The non-dimensional parameters are as follows:

Table 2

Mesh independence test for selected cases.

Case study	Number of elements	St	$\overline{C_d}$
Bare cylinder	1962	0.167	1.35
	4567	0.165	1.34
	8254	0.164	1.33
	17245	0.164	1.33
Bare cylinder with an attached rigid splitter plate	1985	0.139	0.164
	4589	0.137	0.162
	10933	0.136	0.161
	19456	0.136	0.161
Bare cylinder with an attached flexible splitter plate	2017	0.179	1.294
	6446	0.177	1.292
	12745	0.177	1.291
	30830	0.177	1.291
Cylinder with three circular arc plates and two downstream flexible plates at $S^* = P^* = 0.5$	8972	0.116	0.713
	11673	0.117	0.715
	16556	0.118	0.717
	31830	0.118	0.718
Bare cylinder with two downstream flexible plates at $S^* = P^* = 0.5$	8001	0.157	1.152
	10673	0.158	1.153
	15556	0.159	1.157
	30830	0.159	1.158

$$W_z^* = \frac{W_z d}{U_\infty} \quad (29)$$

$$u^* = \frac{u_{rms}}{U_\infty} \quad (30)$$

$$v^* = \frac{v_{rms}}{U_\infty} \quad (31)$$

$$U^* = \frac{\bar{u}}{U_\infty} \quad (32)$$

2.4. Computational mesh

As seen in Fig. 4, an unstructured mesh with triangular elements is employed to discretize the computational domain. The grid becomes finer as it reaches the solid boundaries and meets the requirement of $y^+ < 0.25$. The deformation of the mesh domain with the structural movement is done utilizing the Winslow smoothing method

Table 3
Verification of the flow parameters for bare cylinder and cylinder with an attached rigid plate ($\frac{L}{d} = 1$) at $Re = 100$.

Test case	Bare cylinder			One rigid splitter plate attached to the cylinder	
	St	$\overline{C_d}$	$C_{l_{rms}}$	St	$\overline{C_d}$
Sudhakar and Vengadesan (Sudhakar and Vengadesan, 2012)	0.165	1.37	–	0.139	1.174
Bao and Tao (Bao and Tao, 2013)	0.164	1.335	–	–	–
Kwon and Choi (Kwon and Choi, 1996)	–	–	–	0.137	1.18
Williamson (Williamson, 1989)	0.164	–	–	–	–
Norberg (Norberg, 2003)	0.164	–	0.22	–	–
Hwang et al. (Hwang and Yang, 2007)	0.167	1.34	–	0.137	1.17
Present study	0.164	1.33	0.228	0.136	1.161

for the moving mesh (Knupp, 1999). As provided in Table 2, the flow quantities including the Strouhal number (St) and the mean drag coefficient ($\overline{C_d}$) are considered to evaluate the mesh independence study by four different mesh resolutions. The selected cases are validation cases including bare cylinder, bare cylinder with an attached rigid and flexible splitter plate and also bare cylinder and CAP with two detached splitter plates at $S^* = P^* = 0.5$. According to Table 2, for all cases, the third grids have adequate resolutions to extract other results. Additionally, for the time-independence study, four different time steps of 0.05, 0.01, 0.005, and 0.001s were considered, and accordingly, the results of $\overline{C_d}$ and St were investigated. Finally, a time step of 0.005s was selected to ensure accurate convergence, stability of the solution, and effective computational cost.

2.5. Numerical scheme

The simulation is conducted using COMSOL Multiphysics. In this work, in addition to the characterization of fluid dynamics, the electrical energy harvesting by the piezoelectric deformation is simulated. The fluid-solid interaction is addressed with a fully-coupled FSI problem based on the ALE method (Donea et al., 2004). For the discretization of fluid flow and structure equations, the second-order element and quadratic Lagrange schemes are employed. Direct algorithm with PARDISO solver is implemented. For the moving mesh, the Winslow smoothing method is utilized. Due to the grid flexibility, the time-dependent solver of BDF (backward differential formula) is used to achieve the best CFL (Courant–Friedrichs–Lewy). The second and linear orders are set for the maximum and minimum BDF, respectively.

2.6. Validation

The fluid flow model is verified using the results of flow past a circular cylinder and a rigid splitter plate attached to the cylinder in (Hwang and Yang, 2007; Kwon and Choi, 1996; Norberg, 2003; Sudhakar and Vengadesan, 2012), as provided in Table 3.

With regards to the effectiveness of arc plates on the flow characteristics of a cylinder, investigation of the hydrodynamic forces could be beneficial. According to Fig. 5a, employing arc plates around the cylinder affects the hydrodynamic forces applied on the structural surface. The root-mean-square (RMS) of the lift coefficient ($C_{l_{rms}}$) increases by 23.59% related to a bare cylinder. Furthermore, a 30% reduction in the $\overline{C_d}$ is observed in the CAP related to the bare cylinder case. It is worth noting that the mean drag coefficient and RMS of the lift coefficient for the proposed system (cylinder and three arcs) increases by 26.73% and 66.56% compared to the bare cylinder, respectively. Since the major

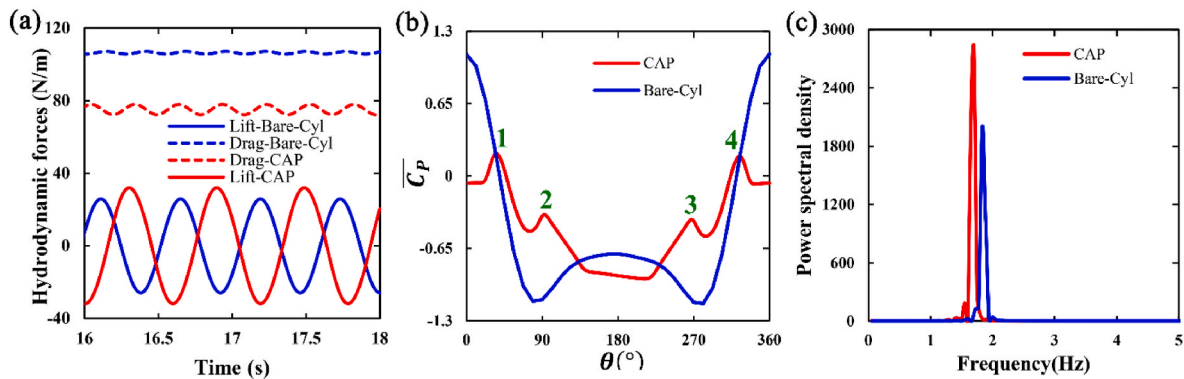


Fig. 5. Comparison of the results of two-cylinder cases with and without implementation of the arc plates; (a) hydrodynamic forces (b) Mean pressure coefficient over the cylinder surface ($\overline{C_p}$) (c) Power spectral density function of the lift force.

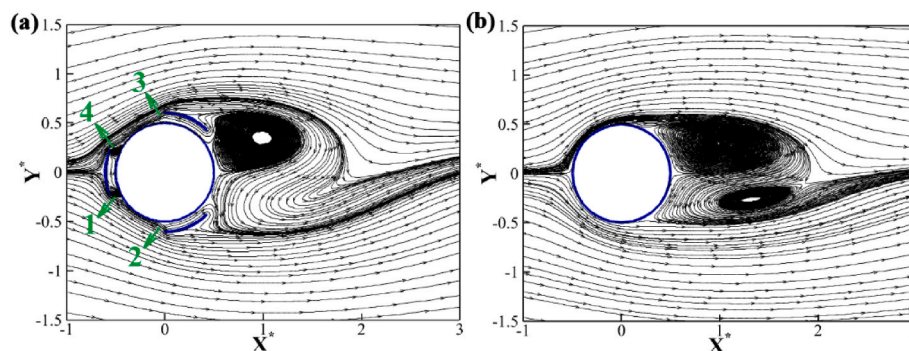


Fig. 6. Time-averaged streamline pattern: (a) CAP, (b) bare cylinder; Points 1, 2, 3, and 4 for the CAP correspond to the points with increased mean pressure coefficient in Fig. 5b.

Table 4
Validation of the results of a flexible splitter attached to the cylinder at $Re = 200$.

Test case	Drag force		Lift force		Plate tip displacement (x)		Plate tip displacement (y)	
	Magnitude (N)	Frequency (Hz)	Magnitude (N)	Frequency (Hz)	Magnitude (mm)	Frequency (Hz)	Magnitude (mm)	Frequency (Hz)
Turek and Horn (Turek and Hron, 2006)	149.78 ± 2.22	10.9	457.3 ± 22.66	5.3	-2.69 ± 2.53	10.9	34.38 ± 1.48	5.3
Present study	150 ± 4.49	10.41	454 ± 24.8	5.31	-2.7 ± 2.5	10.45	33.50 ± 0.5	5.35

part of the drag coefficient is the pressure drag, to better understand the underlying mechanism of drag reduction, the mean pressure coefficient ($\overline{C_p}$) is plotted on the cylinder surface in Fig. 5b θ is the angle along the cylinder surface which is determined from the front stagnation point ($\theta = 0^\circ$ or 360°). As seen, the pressure changes within a narrower range when arc plates are added; hence, a lower drag coefficient is obtained. Moreover, the frontal arc plate decreases the $\overline{C_p}$ in the front stagnation point of the cylinder and as a result, the effective drag reduces. In addition, noticing the pressure variation, the base pressure coefficient decreases compared to the bare cylinder (Fig. 5b at $\theta = 180^\circ$).

Fig. 5c indicates the power spectral density function of the lift force for both cylinder cases. The frequency assessment shows that the frequency decreases from 1.848 Hz to 1.690 Hz, consequently, the Strouhal number declines by 8.54%.

The time-averaged streamlines are plotted for the CAP and the bare cylinder in Fig. 6. For CAP, the wake region includes one strong vortex in the vicinity of the cylinder. The center of this vortex is associated with a low-pressure region. So, parts of the cylinder surface that interacts with these vortices have low $\overline{C_p}$. The absence of the second vortex formation in the back of the CAP surface causes a pressure gradient at $135^\circ \leq \theta \leq 225^\circ$. However, for the bare cylinder, two vortices are generated in the wake region leading to higher oscillations. Moreover, for the CAP, two tiny vortices are generated in the space between the frontal arc and the cylinder surface. Based on this, at points 1 and 4 in Fig. 5b and 6a, two peaks in the mean pressure coefficient can be detected. Furthermore, an enhancement of this coefficient can be detected at points 2 and 3 owing to the impacts of the upper and lower arc plates in the passing fluid flow.

Additionally, to validate the simulation of flexible plates, the results of an attached flexible plate to the cylinder are compared with the experimental results of Turek and Horn (Turek and Hron, 2006). Based on this, Table 4 provides comparisons for the frequency and magnitude of drag and lift forces, as well as the tip displacement of the flexible splitters. As can be seen from Tables 3 and 4, the present numerical results are in agreement with the relevant studies.

For the energy harvesting results, the average electrical power of a cantilever beam is investigated under a base excitation with the classical experimental results of Erturk and Inma (Erturk and Inman, 2011) and Priya and Inman (2009). The corresponding electrical power of the

present study is $0.5 \frac{mW}{m}$, which is in close agreement with the experimental data reported by (Erturk and Inman, 2011; Priya and Inman, 2009).

3. Results and discussion

Downstream vortex shedding has a destructive effect on the circular structure due to the VIV, which makes it crucial to control the wake formation using control methods. The design of control methods is based on the flow structure and characteristics of the wake region. Therefore, in this section, the design parameters are selected based on comparisons of hydrodynamic parameters targeting at reducing the drag and the lift fluctuations. Additionally, the impact of the design parameters is evaluated on the energy harvesting from the VIV to maximize the level of the harvested energy.

3.1. Wake control results

Variations of the Strouhal number against of S^* for the CAP with downstream flexible plates are demonstrated in Fig. 7a and compared with the results of our previous study for the bare cylinder (Eydi et al., 2022) in Fig. 7b. The case of a single splitter is also presented along with double splitters simulated at different pitch (S^*) values. Comparing the two figures for the limiting case of no plates, one notes a drop in the St. The frequency assessment in Section 3.1. showed that the wake suppression is improved by adding circular arc plates to the cylinder. Thus, it is expected that by combining the effect of arc plates with flexible splitter plates as a passive control method, the Strouhal number will decrease dramatically. However, according to Fig. 7a, there is an exception for the single plate case for which the Strouhal number exceeds that of the CAP at $S^* \leq 0.5$. This can be attributed to a tiny vortex known as the tip vortex that formed near the tip of the splitter (Eydi et al., 2022). It communicates with the main vortices and increases the flow instability as it approaches the CAP. Also, there are enhancements in the St of bare cylinders followed by a single plate at $S^* \leq 0.5$, and followed by dual splitter plates at $S^* = 0$ and $2 \leq P^* \leq 3$.

For a single plate, the highest values of the Strouhal number for both CAP and bare cylinder are pertinent to the case of an attached plate ($S^* = 0$); these maximum values are 7.27% and 7.93% higher than those

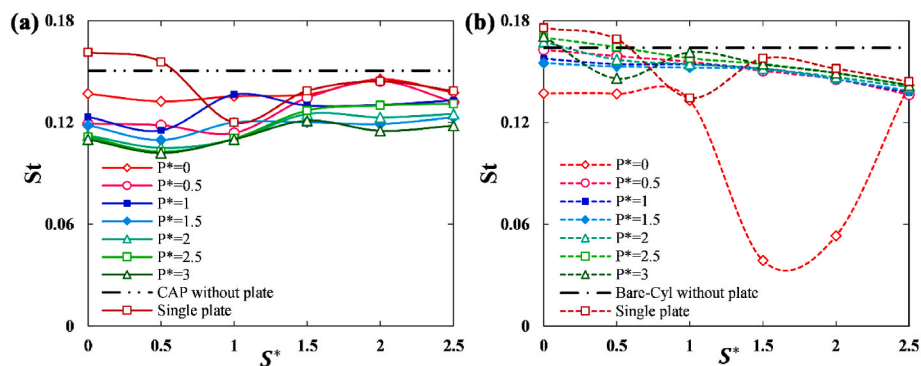


Fig. 7. Variation of the Strouhal number for cylinder cases with single and dual splitters at different S^* and P^* : (a) cylinder with arc plates (CAP), (b) bare cylinder (Eydi et al., 2022).

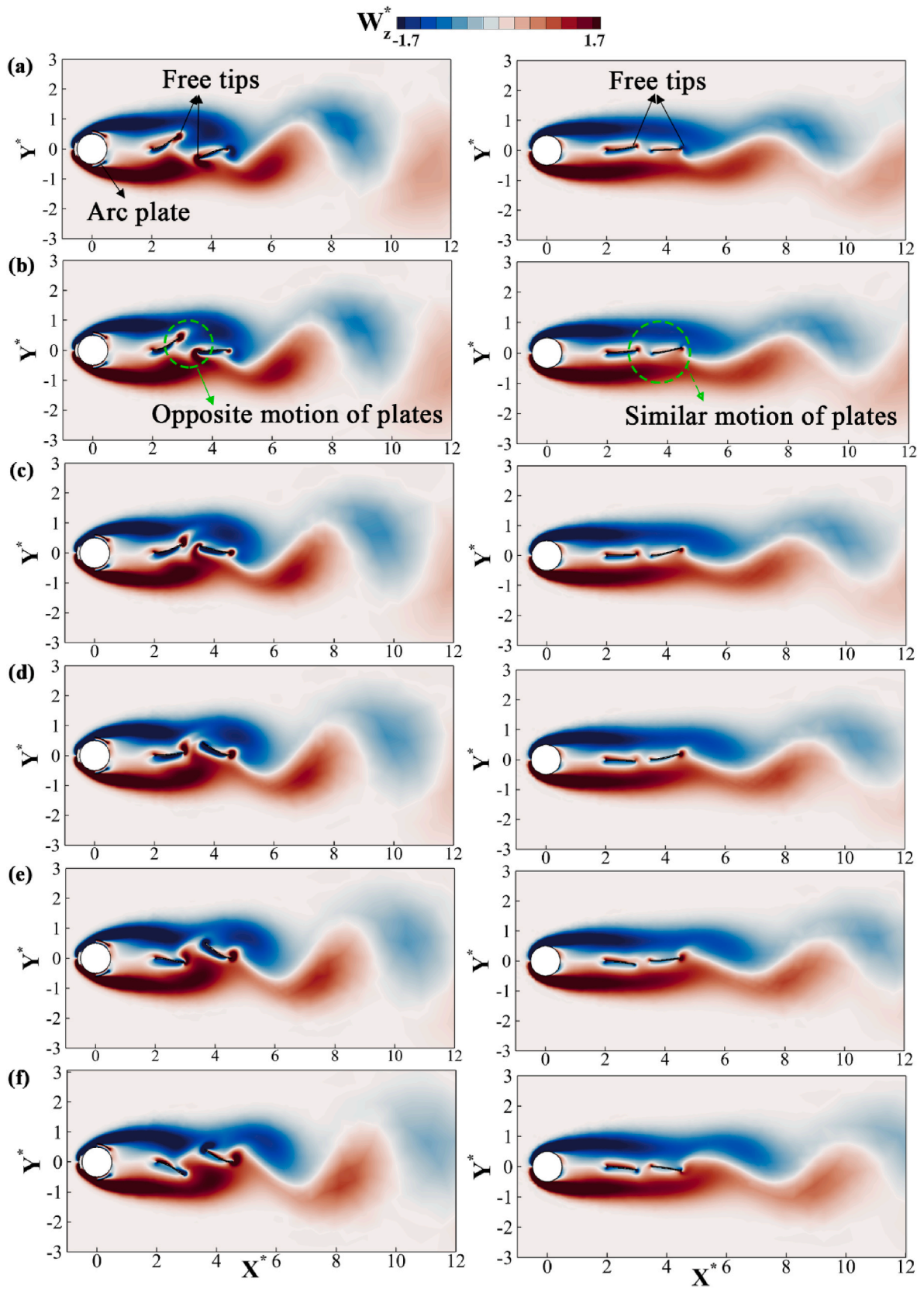


Fig. 8. Instantaneous non-dimensionalized spanwise vorticity contours (W_z^*) during a half cycle of dual detached flexible plates: (a)–(f) present 0T, 0.1T, 0.2T, 0.3T, 0.4T, and 0.5T, respectively, where T is the period. Left column: CAP with splitters, Right column: bare cylinder with splitters. The splitters are located at $S^* = 1.5$ and $P^* = 0.5$.

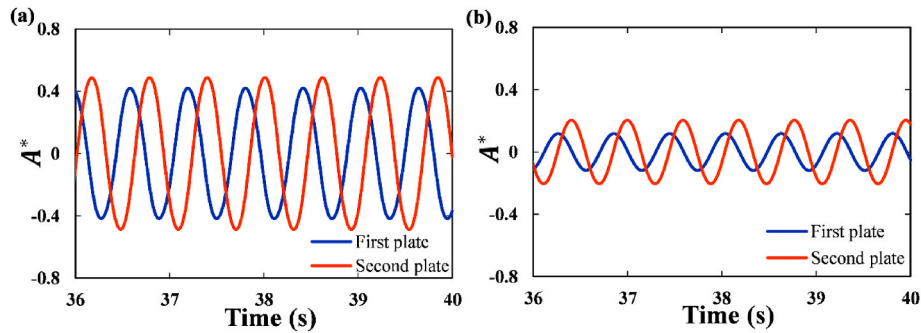


Fig. 9. Time histories of vibration amplitudes of the first and the second flexible splitter plates: (a) CAP, (b) bare cylinder, for $S^* = 1.5$ and $P^* = 0.5$.

of no-plate cases, respectively. One notes that the same trend was observed by Abdi et al. (2019).

According to Fig. 7, for all investigated cases, the results of CAP are more promising than those of the bare cylinder, except for dual plates with $P^* = 0$ and $1 \leq S^* \leq 2$. The most notable reduction in the Strouhal number for dual-splitter plates in CAP and bare cylinder occurs when $S^* = 0.5$, $P^* = 3$ and $S^* = 1.5$, $P^* = 0$, respectively. As a result, the Strouhal numbers are 37.80% and 76.35% lower than that of the bare cylinder. It can be seen that the performance of designs with dual plates is ubiquitously better than those of single plates for the CAP and the bare cylinder.

Fig. 8 demonstrates the instantaneous non-dimensional spanwise vorticity contours (W_z^*) for the CAP and the bare cylinder followed by dual flexible plates during a half cycle of shedding, at $S^* = 1.5$ and $P^* = 0.5$. The cycle's starting (0T) corresponds to the maximum deformation of the first splitter plate. The development of two distinct shear layers in the voracity contours is evident.

Different periodic oscillation regimes of two splitter plates are observed especially for the CAP case. The vibrating harmonic oscillations driven by alternating low-pressure vortices lead to different periodic regimes of flexible splitter plates for the CAP and bare cylinder cases. The local pressure difference across the plates causes periodic traveling wave-type deformations of splitters. It is noticeable that the splitters of the CAP move in the opposite direction due to the positions of the shear layers, while the splitters of the bare cylinder move in the same direction.

Fig. 9 displays the time histories of vibration amplitudes for both plates in mentioned configuration, where $A^* = \frac{A}{D}$ denotes the maximum plate deformation which is anticipated to be observed at the free tip of the plate. It is observed that with both CAP and bare cylinder, the second plate's amplitude is greater than the first plate because of the more frequent and severe shear layer presence downstream. Nonetheless, for the CAP, fixing the end of the second plate also triggers more oscillations. Furthermore, assessments of the normalized tip amplitude (A^*) reveal that the CAP plates have a larger amplitude compared with the bare cylinder because the shear layers interact more strongly. As a result, a considerable increase in tip amplitude, about 183%, compared with the bare case improves the energy harvesting performance.

The implementation of flexible splitter plates suppresses vortex shedding (Murali and Petha Sethuraman, 2024). Accordingly, using splitters in the proposed case of bare cylinder leads to an 8.53% decrease in the Strouhal number. Here, combining the arc plates with flexible splitters results in a noticeable reduction of 18.29% in the St compared with the bare cylinder case. For a more comprehensive understanding of the problem, streamlines are demonstrated for a half cycle of plate oscillations in Fig. 10.

In the vortex shedding process, the vortex formation and inter-vortex distances between consecutive vortices determine the Strouhal number. Hence, the horizontal distance between the positive and negative peaks of two successive vortices is measured for the CAP and bare cylinder

cases and it is denoted by " D_{SV} ". It is observed that D_{SV} is longer for the CAP than the bare cylinder. In fact, in the CAP, one strong peak appears adjacent to the cylinder while the second strong vortex appears further away in the vicinity of the splitter plates. However, for the bare cylinder, both of the strong vortices are generated in the cylinder-first plate gap spacing at a shorter distance. These observations confirm the smaller Strouhal number for the CAP case related to the bare cylinder. Additionally, for the CAP, the proximity of the second strong vortex between the plates provides more propulsion and consequently higher tip amplitude. Moreover, as demonstrated by the streamline pertinent to the CAP case, the separation of tiny vortices in the vicinity of the plates' tips is slower compared with the bare cylinder, illustrating higher flow instability of the plates. All of these factors contribute to an improved wake control and enhanced energy harvesting capacity for the CAP case compared with the bare case.

To explore the dynamics of mean wake flow, non-dimensional contours of RMS streamwise and transverse velocities (u^* and v^*) at different S^* ($0 \leq S^* \leq 2.5$) and fixed P^* ($P^* = 0$) are provided in Figs. 11 and 12. In this study, employing the splitter plates diminishes the level of velocity fluctuations and consequently suppresses vortex shedding. According to Fig. 11, there are peaks in u^* based on the plates' positions, corresponding to the roll-up locations of the shear layers. Notably, in the case of a bare cylinder, two symmetric peaks appear in the wake area of the second splitter. However, in the case of CAP, two additional symmetric peaks form between the two plates due to the specific flow characteristics. As shown in Fig. 11, both cases show a higher potential for the rolling up of shear layers after the location of the second splitter plate. However, this potential is higher in the case of CAP. Subsequently, the rolling of shear layers grows strongly with the introduction of arc plates, showing more disturbance. The strongest peaks are observed for the CAP and bare cylinder cases at $S^* = 0.5$ and $S^* = 2.5$, respectively. The distinct feature of u^* contours based on the S^* is due to the specific interaction of vorticities. Furthermore, the lateral distance between the two peaks, known as the wake width, becomes lower with the inclusion of the splitter plates. At the same time, a lower wake width corresponds to a lower drag coefficient. In contrast to u^* contours, there are single or multiple strong peaks in the middle wake region of the cylinders, depending on the numerical value of S^* , as displayed in Fig. 12. v_{rms} evaluates the interaction between wake vortices and also the trend of v_{rms} indicates alterations in the lift force. Tracing the location of large peaks, they are captured at the leading edge of the second splitter, and at downstream, where vortices are freely formed. Similar to the u^* contours, stronger peaks of v^* are observed in the CAP cases compared to bare cylinder cases. This is due to the effect of arc plates in increasing the lift coefficient which significantly influences on v_{rms} . The highest peaks of v^* are observed for the CAP and bare cylinder cases at $S^* = 0$ and $S^* = 2.5$, respectively.

For three cases of bare cylinder with dual plates ($S^* = 1, 1.5, 2$), numerical values of both transverse and streamwise velocity fluctuations (u^* and v^*) are very small, and no peak is captured for attached

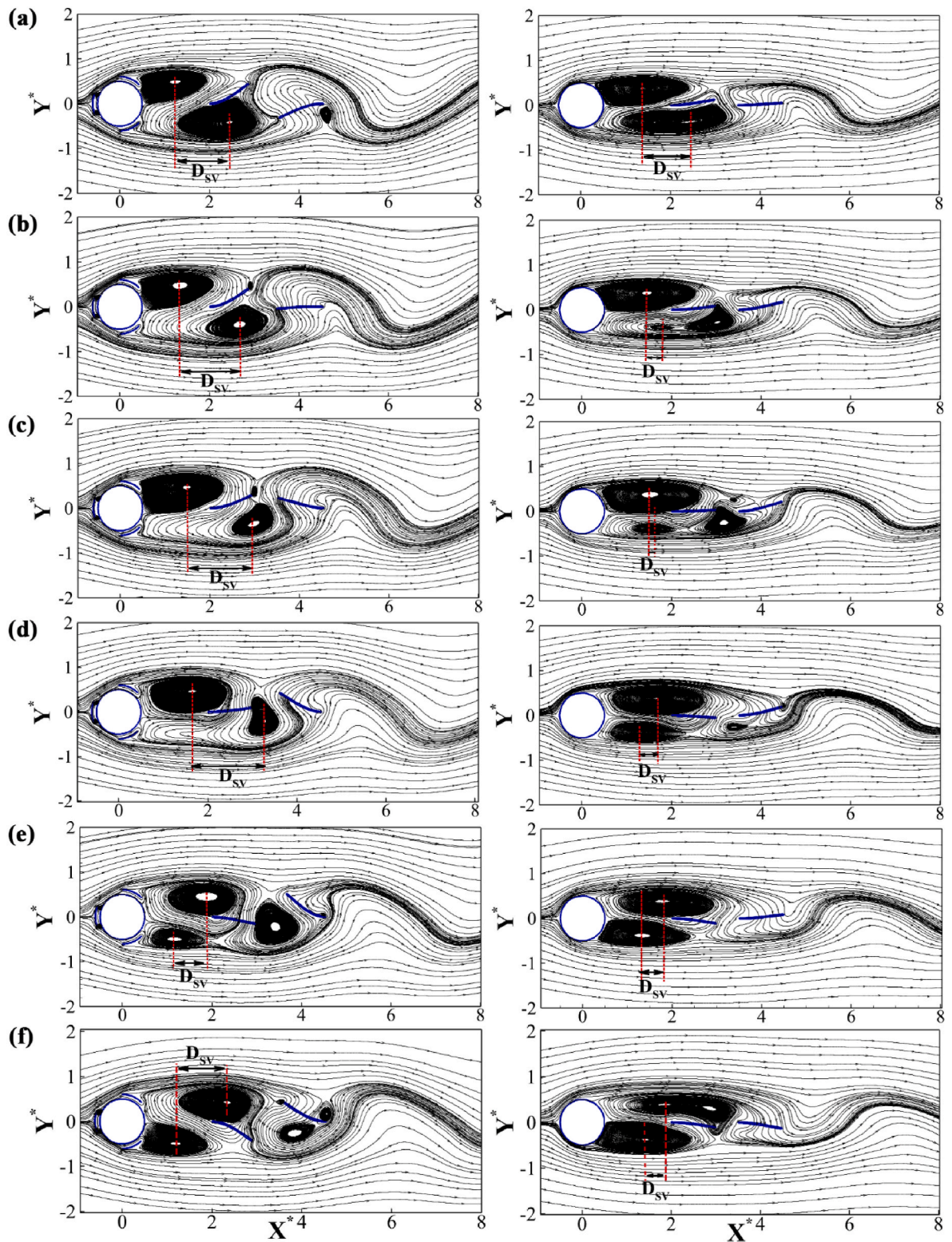


Fig. 10. Streamline patterns for a half cycle of dual plates ($S^* = 1.5$ and $P^* = 0.5$): (a)–(f) present $0T$, $0.1T$, $0.2T$, $0.3T$, $0.4T$, and $0.5T$, respectively, where T is the period. Left column: CAP, Right column: bare cylinder; D_{SV} is the horizontal distance between two successive vortices.

plates ($P^* = 0$) as demonstrated by Figs. 11 and 12. This is because of the limited communication between shear layers imposed by the splitter plates. As a result, shear layers shed independently of one another, and velocity fluctuations become insignificant. The control performance of the bare cylinder cases is better compared to the CAP cases only with $P^* = 0$, as mentioned before. Thus, the rate of velocity oscillation

reduction is improved for these cases.

RMS contours of static pressure (P_{rms}) is depicted in Fig. 13. In the vortex shedding process, alternating vortices are shed from either side of the centerline, while their centers have low pressure. Therefore, vortices are shed in the low-pressure region while much higher pressure is observed across the other side of the plate. As a result, pressure

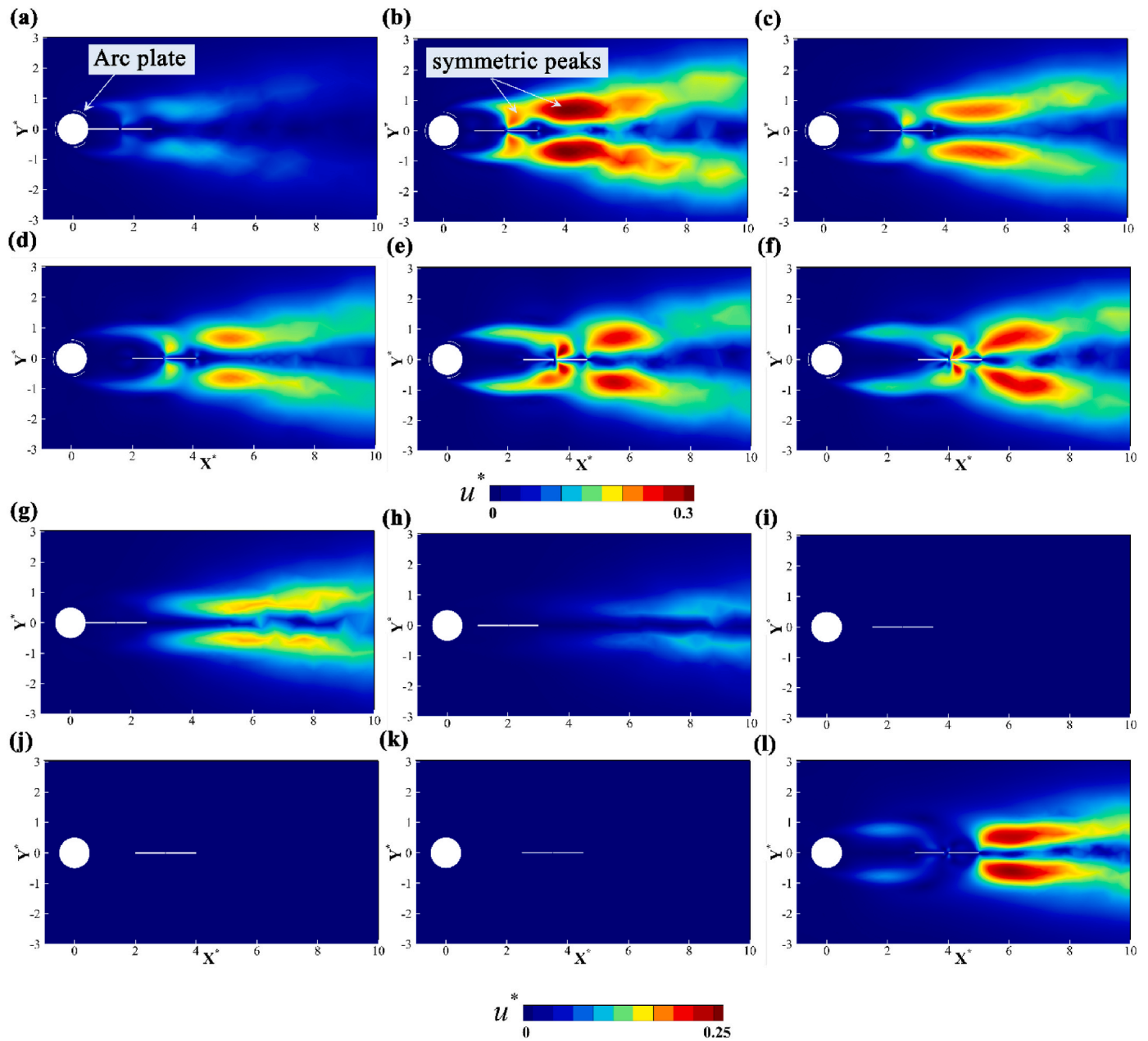


Fig. 11. Non-dimensional contours of RMS streamwise velocities (u^*) for two-cylinder cases with dual splitters at fixed $P^* = 0$ and at different $S^* = 0, 0.5, 1, 1.5, 2$ and 2.5 : (a)–(f): CAP, (g)–(l): bare cylinder.

fluctuations occur. As seen, the wake region, where vortices are generated, exhibits the highest pressure fluctuations.

With both cylinder cases, P_{rms} decreases compared to the cylinder without any splitters. Furthermore, as Fig. 13 depicts, bare cylinder cases are associated with lower P_{rms} compared to the CAP cases. Additionally, for two cases of CAP, at $S^* = 2$ and $S^* = 2.5$, region at the vicinity of the second plate involves a high-pressure gradient. The same high-pressure zone for bare cylinder cases is observed at $S^* = 0$ and $S^* = 2.5$ downstream the second splitter plate. As previously displayed in Figs. 11 and 12, pressure fluctuations are negligibly small for three cases of bare cylinder with dual plates ($S^* = 1, 1.5, 2$).

The oscillations of drag and lift forces play a major role in the physical aspects of the VIV, which is a key factor for the fatigue failure of the structure. Thus, variations of the mean drag coefficient ($\overline{C_d}$) and the RMS of the lift coefficient ($C_{l,rms}$) against S^* are depicted in Fig. 14a and b and compared with those of the bare cylinder reported in our previous

study (Eydi et al., 2022). The results of CAP and bare cylinder without flexible splitter plates are also included. Both graphs display a significant reduction in $\overline{C_d}$. Comparing the two graphs, one observes that combined effects of arc and flexible plates are more efficient in drag reduction. By combining the effect of arc plates and dual detached splitters ($S^* = 0.5, P^* = 3$), significant drag reductions of 53.3% and 34.0% can be achieved compared with the bare cylinder and CAP, respectively. Comparatively to the results reported in (Bao and Tao, 2013; Chehreh and Javadi, 2018; Hwang and Yang, 2007), the performance of the proposed structure is greatly improved. Furthermore, $C_{l,rms}$ can be used as an indicator to assess the effectiveness of wake control. As mentioned before in Section 3.1 A, arc plates lead to 23.59% enhancement in the RMS of the lift coefficient related to the bare cylinder. However, for both cylinder cases, the implementation of splitter plates leads to a dramatic reduction and even complete suppression of $C_{l,rms}$. Fig. 14c illustrates how the base pressure coefficient varies on the

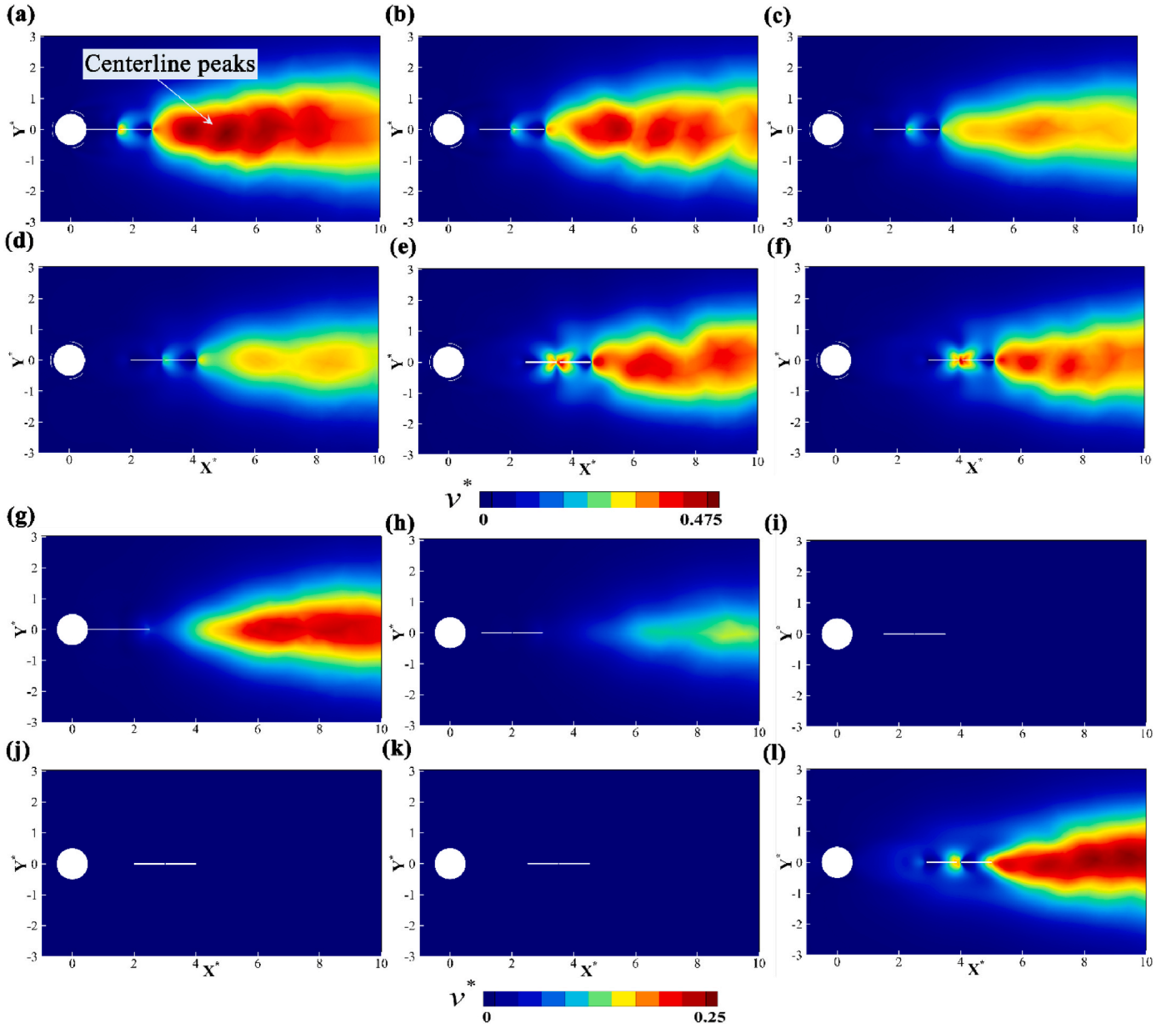


Fig. 12. Non-dimensional contours of RMS transverse velocities (v^*) for two-cylinder cases with dual splitters at fixed $P^* = 0$ and at different $S^* = 0, 0.5, 1, 1.5, 2$ and 2.5 : (a)–(f): CAP, (g)–(l): bare cylinder.

cylinder surface. One observes that the numerical value of $-\overline{C_{pb}}$ for all cases considered here within the newly-proposed design (different S^* and P^*) has a lower value than that of the cylinder cases. The results show the same trend as $\overline{C_d}$ (Fig. 14a). This strong correlation of $\overline{C_d}$ and $-\overline{C_{pb}}$ for bluff bodies can be explained by the predominance of pressure drag over viscous drag.

For an inclusive interpretation of the results, the effect of changing S^* on the non-dimensional mean streamwise velocity (U^*) for a single flexible splitter is studied with results reported in Fig. 15. Comparison of the contours shows that increasing S^* , expands the low-velocity and high-pressure zone downstream of the cylinder, causing a reduction in the drag related to both cylinder cases.

3.2. Energy harvesting results

In this section, the electricity generation characteristic of the proposed design is investigated. Hence, the location of splitters is para-

metrically varied, and numerical simulations are performed for each case. In response to the lift force fluctuations, the flexible plate bends and undergoes a periodic wave-type deformation. The maximum amplitude of oscillations is observed at the plate tip and can be achieved through the vertical component of vector deformation (u_s) in Eq. (6). Fig. 16 demonstrates the total non-dimensional plate tip amplitude ($A^* = \frac{A}{B}$) versus S^* . In both cases, the amplitude of splitters is highly sensitive to different arrangements. Also, in the majority of cases, measurement of A^* shows dual plate cases have a higher amplitude than those with single plate. For dual plates of CAP, the overall trend of A^* with increasing S^* is ascending. Hence, the highest amplitude at different pitch (P^*) values occurs at $S^* = 2.5$. The displacement values significantly increase, about four times, for dual plates compared with that of a single plate at $S^* = 2.5$.

For the bare cylinder case, the amplitudes of dual plates are zero at fixed $P^* = 0$ and $1 \leq S^* \leq 2$, which is consistent with $C_{l_{rms}}$ (Fig. 14b), due

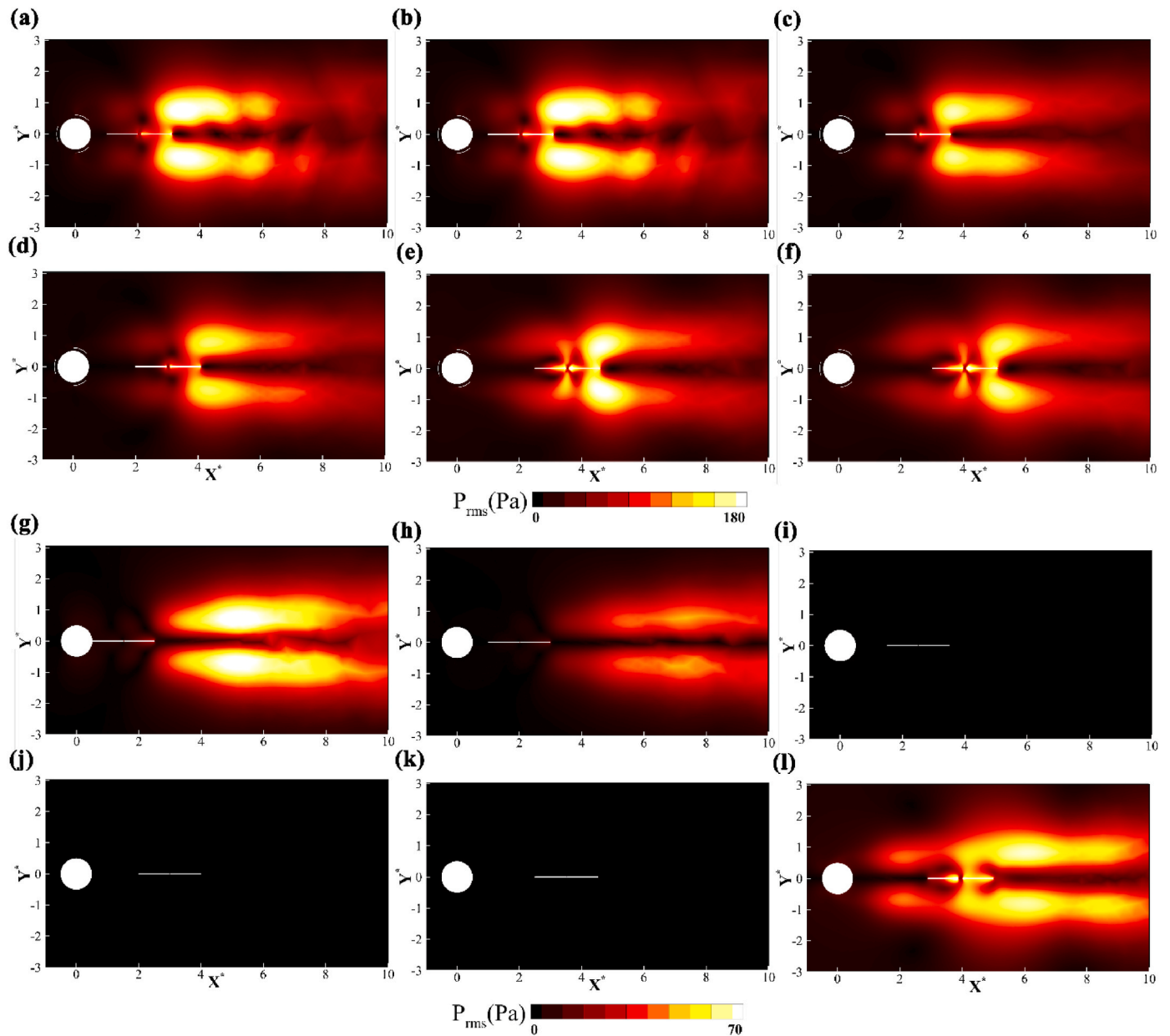


Fig. 13. Contours of static pressure (P_{rms}) for two-cylinder cases with dual splitters at fixed $P^* = 0$ and at different $S^* = 0, 0.5, 1, 1.5, 2$ and 2.5 : (a)–(f): CAP, (g)–(l): bare cylinder.

to a symmetric pattern of shear layers relative to the wake centerline, the splitter plates do not experience any vertical force. Comparing the results for single and dual plates, at $S^* = 1$, one notes an almost 18-fold increase in the amplitude for the latter case compared with the former.

The Strouhal number is closely linked to the oscillatory behavior of the flow, which affects the amplitude of the oscillations. The St value directly influences the flapping amplitude, which in turn impacts the efficiency of energy harvesting. In this study, the effect of varying St across different P^* and S^* is analyzed to observe how it affects the flow characteristics and the flapping amplitude. Variations in St are expected to be closely associated with variations in amplitude, directly affecting energy harvesting efficiency. Therefore, utilizing this integrated approach the present study thoroughly considers the combined influence of St and amplitude on energy harvesting.

One notes that for both CAP and bare cylinder cases followed by a single plate, the Strouhal number (Fig. 7) shows a similar trend to A^* in Fig. 16. When the tip displacement is higher, it results in greater

instability and consequently leads to a higher Strouhal number. Additionally, dual splitter plates have different tip amplitudes due to the complex shedding mechanism and the negligible impact of plates on cylinder oscillation farther downstream. Comparison of Fig. 16a and b shows that the inclusion of arc plates has a strong effect on the plate displacement amplitude.

The PEHs are capable of producing electrical charges when pressure or strain is applied to them (Ramadan et al., 2014). Hence, a crucial factor in producing power from PHEs is the material strain. To ensure the adequacy of the proposed method for energy harvesting, the contour plot of the maximum strain (ϵ_{max}) for different configurations is shown in Fig. 17. In fact, utilizing the maximum displacement values in Fig. 16, the strain can be computed by taking the flexible plates as a cantilever beam. The results of both graphs reveal that in the majority of cases, the strain is higher with CAP. It is accomplished by imposing a fixed boundary condition on the trailing edge of the second plate, which facilitates the deformation along with the implementation of the arc

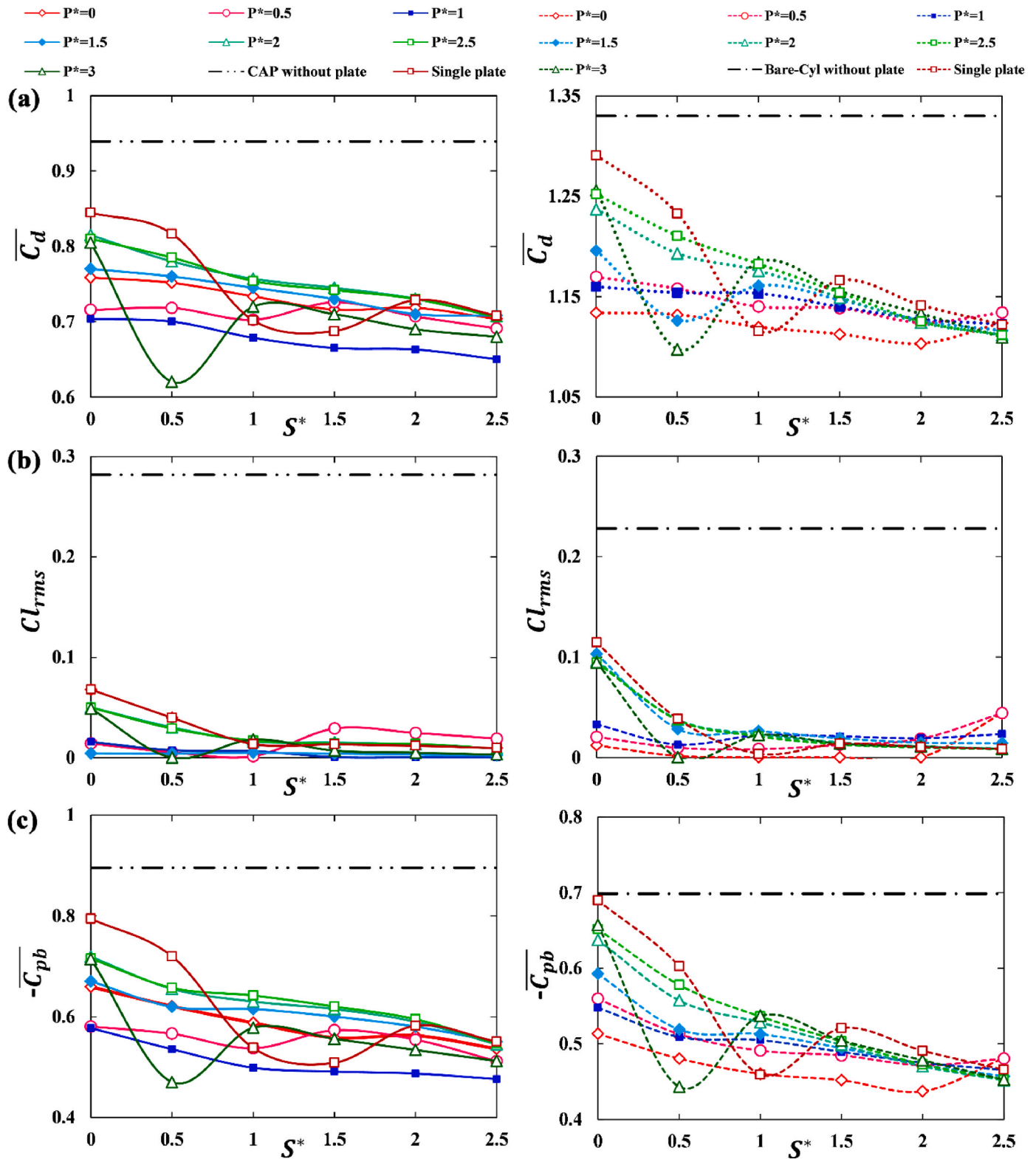


Fig. 14. Hydrodynamic parameter of wake control at different arrangements of flexible plates. (a) mean drag coefficients ($\overline{C_d}$), (b) RMS of lift coefficient ($C_{l_{rms}}$), (c) time-averaged base pressure coefficient ($-C_{pb}$); Left column: CAP, Right column: bare cylinder (Eydi et al., 2022).

plates.

Different results are obtained at different P^* values as one would expect. For all cases of the bare cylinder, the highest strain is related to dual splitters within the range of $1.5 \leq P^* \leq 3$ at $S^* = 0$. In the presence of arc plates, this range is further limited to $1.5 \leq P^* \leq 2.5$, but the

optimal results are shifted to the other end of S^* extremes, i.e. $S^* = 2.5$, which has a significant enhancement of 170.2% compared with the highest strain pertinent to a bare cylinder. For single plate of CAP, the highest strain occurs at $S^* = 0.5$ with about 29.0% rise compared to the top strain of bare cylinder cases (single plate at $S^* = 0$).

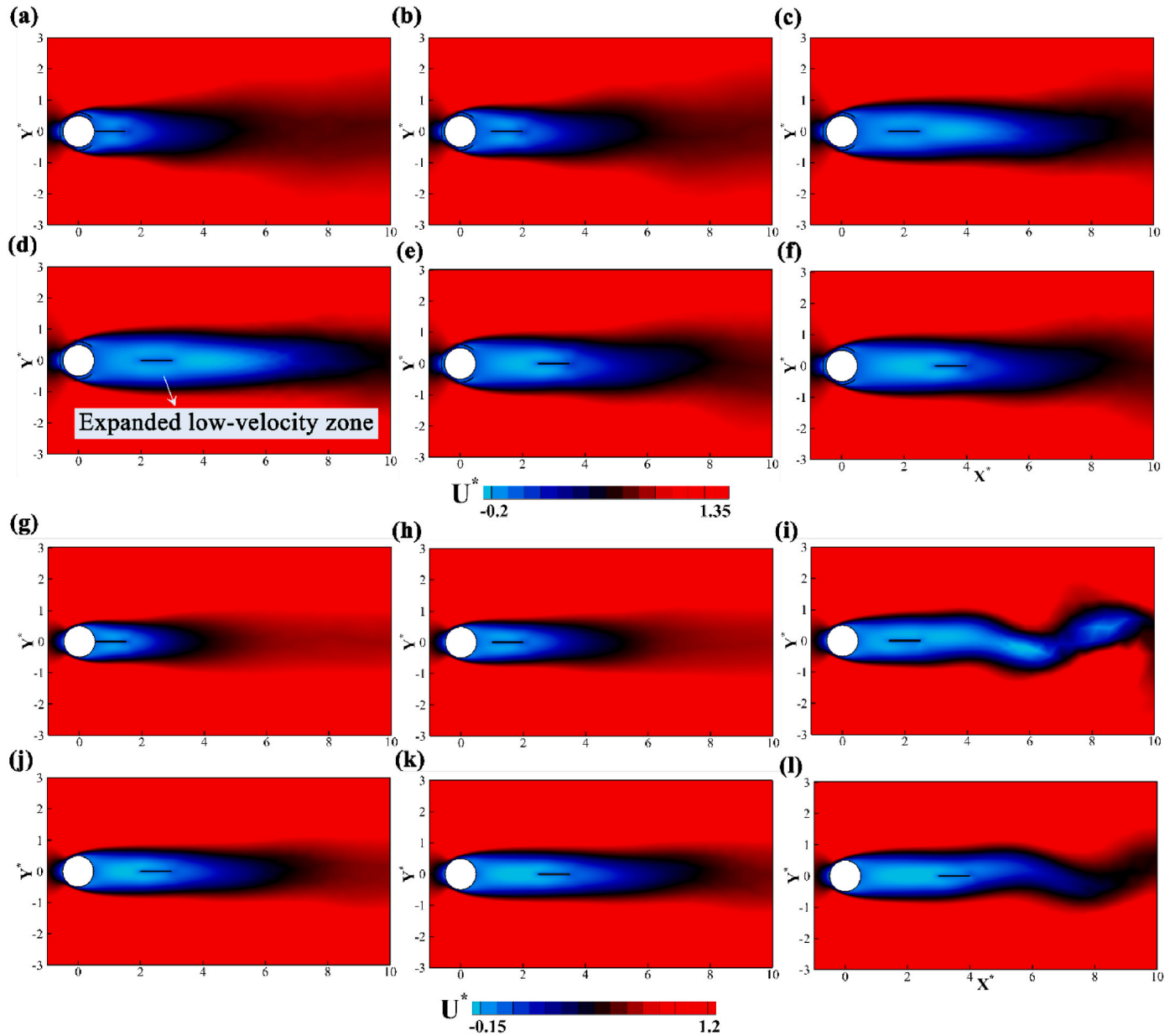


Fig. 15. Contours of non-dimensional mean streamwise velocity for two-cylinder cases with single splitters at different $S^* = 0, 0.5, 1, 1.5, 2$ and 2.5 : (a)–(f): CAP, (g)–(l): bare cylinder.

Fig. 18 shows the average electrical power generated by both cylinder cases, bare cylinder and CAP, followed by those with single and dual plates. The resonant flow speed of VIV is very low at a Reynolds number of 100, which considerably limits the generated power from bluff body vibration.

According to the results, for cylinder-based harvester, the average power increases from $0.34 \mu W$ to $0.90 \mu W$ by doubling the number of plates at $S^* = 2.5$. It is even more interesting that by adding the circular arc plates in the same configuration, the electrical power is further enhanced from $0.79 \mu W$ to a peak value of $3.13 \mu W$. In comparison to the bare cylinder case, this is an order of magnitude higher.

The power conversion factor (η) (Barrero-Gil et al., 2010; Ding et al., 2016) is calculated to assess the efficiency of energy harvester systems at various configurations. Fig. 19 illustrates the efficiency of single and dual plates for two-cylinder cases. As seen, the efficiency of the case without arc plates is quite low. High efficiency in CAP is achieved by high harvested power.

For dual plates of CAP-based energy harvester, the efficiency in-

creases with the non-dimensional gap distancing between the CAP and the first plate (S^*). Conversely, in most cases of cylinder-based harvesters, with increasing S^* , the efficiency decreases. Since, by increasing the non-dimensional distance of splitter plate from the bare cylinder (S^*), the shedding process becomes weaker which provides lower vibrational energy for strain. Consequently, the output voltage which affects the efficiency decreases.

On the other hand, no matter the base excitation of the harvester is CAP or bare cylinder, maximum efficiency is achieved at $1.5 \leq P^* \leq 2.5$. So, from the energy point of view, for the optimal placement of the PEHs, the novel proposed structure of the arc plates followed by dual flexible splitters is suggested.

In conclusion, it can be claimed that the proposed structure of circular arc plates integrated with downstream splitter plates while $S^* = P^* = 2.5$ is an optimal configuration, which provides high efficiency of 77.7% and a considerable drag reduction of 46.9% compared to the uncontrolled case.

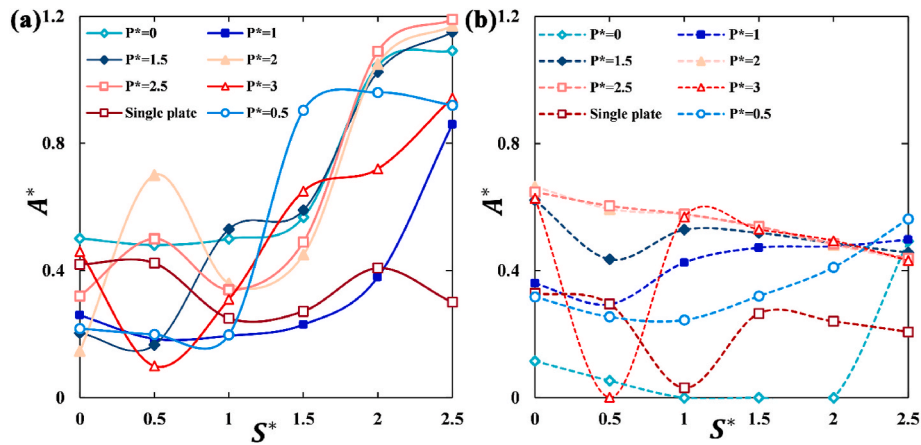


Fig. 16. The total non-dimensionalized tip amplitude (A^*) against S^* for two-cylinder cases with single and dual flexible splitters: (a) CAP, (b) bare cylinder (Eydi et al., 2022).

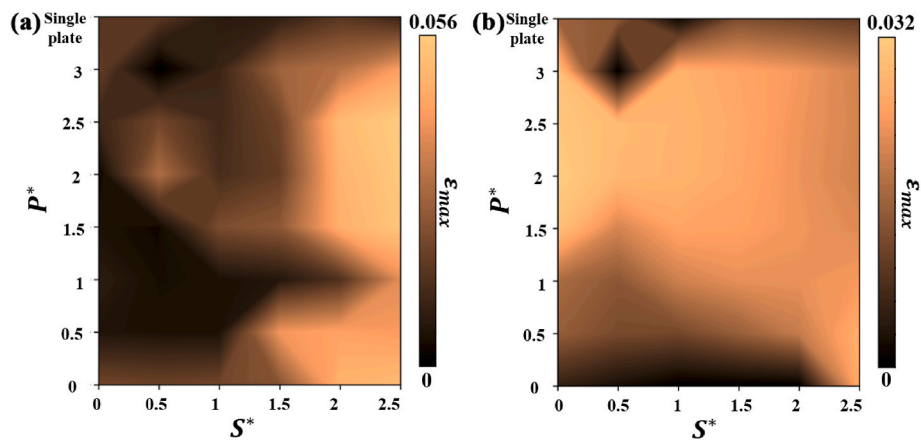


Fig. 17. Variation of the maximum strain (ϵ_{max}) of single and dual flexible splitters against S^* : (a) CAP, (b) bare cylinder.

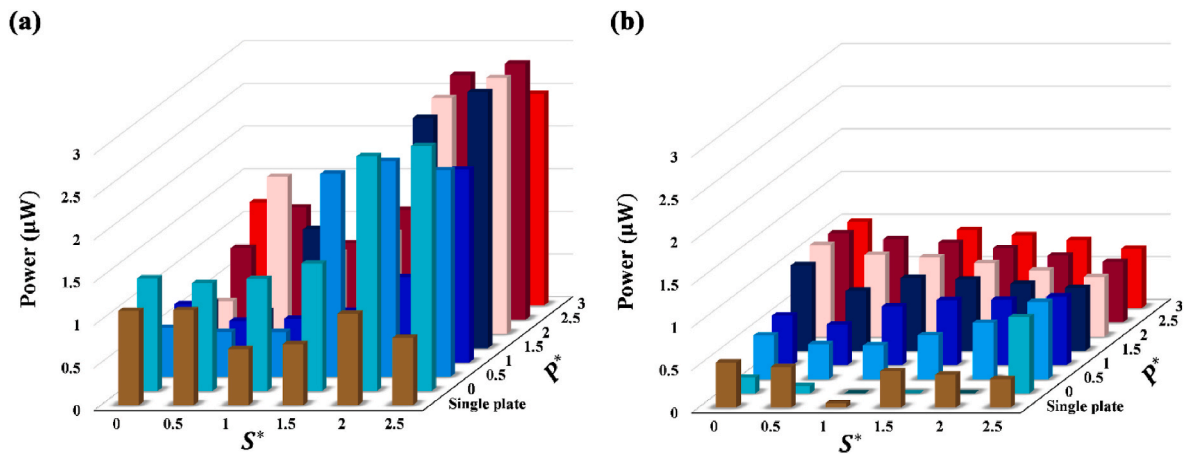


Fig. 18. The average harvested electrical power of the energy harvesters for two-cylinder cases: (a) CAP, (b) bare cylinder.

There are inherent inaccuracies and uncertainty in any numerical simulation of any continuum problem due to discrete approximation, iterative convergence methods, and numerical limitations. The limitations of this study, include the use of 2D simulations instead of 3D models and the inability of the laminar model to accurately evaluate the separation point, potential errors in discretization, and Round-off Errors. Additionally, we acknowledge the limitations of the present study,

particularly regarding the use of a Reynolds number ($Re = 100$) in 2D simulations. While this specific flow regime may not directly relate to offshore, naval, or aerodynamic applications, the methodology and findings can potentially be extended to scenarios with higher Reynolds numbers where turbulent flows are more prevalent. Although $Re = 100$ may not be directly applicable to the mentioned industries, the insights from this study provide a foundational understanding that could be

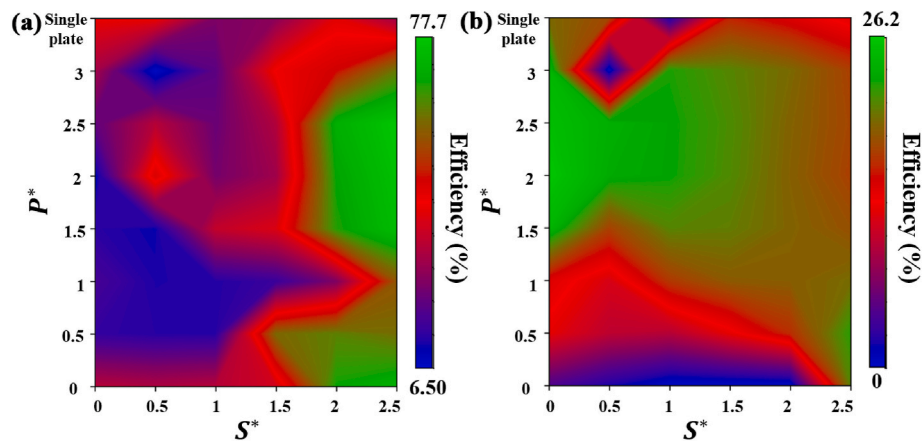


Fig. 19. Efficiency of the energy harvesters in different arrangements: (a) CAP, (b) bare cylinder.

adapted and applied in more complex and larger-scale contexts involving turbulent flows, offering valuable contributions to broader engineering and fluid dynamics applications. To further improve this study, it is recommended to conduct this study in experimental settings and at higher Reynolds numbers, which are more applicable to engineering. Moreover, it would be beneficial to perform a comparative analysis of different configurations using various numbers of arc plates for future research. This analysis should take into account different coverage angles, positions, and the normalized radius of the arc plates to determine the best configurations. Additionally, to enhance the energy harvesting performance, it would be helpful to optimize the amount of resistance load.

4. Conclusions

The technological development of microelectronics has led to the enhancement of the demand for small-scale energy harvesting. The PEHS utilizing flexible splitters in circular structures with wide application in the energy industries can supply this energy. Therefore, this paper numerically studies the energy harvesting of a circular cylinder utilizing three arc plates in the circumferential space around a cylinder. The target is to improve wake control, as well as increasing the energy harvesting potential. To achieve this aim, downstream flexible splitter plates with approved performance are combined with circular arc plates in the form of single and dual configurations.

Results show that equipping the cylinder with arc plates (CAP) in the absence of splitters is hydrodynamically helpful. However, the RMS of the lift coefficient increases for the energy harvesting targets. By adding flexible splitters to the CAP, the hydrodynamic performance is improved.

Evaluation of the control performance of two-cylinder cases with splitter plates shows that the corresponding results of CAP are more promising than bare cylinder except for dual plates at $P^* = 0$ and $1 \leq S^* \leq 2$. Moreover, it is found that in both cases, the control performance of dual plates compared to single plate is improved. Based on this, the Strouhal number for the bare cylinder case with dual plates at $S^* = 1.5$ and $P^* = 0$ is dramatically reduced by 76.35%.

Additionally, a significant drag reduction of 53.3% occurs for the CAP with dual-splitters at $S^* = 0.5$ and $P^* = 3$ in comparison to the bare cylinder.

From the energy harvesting point of view, it is found that the arc plates have a strong impact on the plate displacement amplitude. The increase of the plate displacement is more noticeable for dual splitters than single plate. Additionally, strain assessments show that the highest captured strain belongs to the CAP case, with an increase of 170.2% relative to the top performance of the bare cylinder case. For the cylinder-based harvester, by increasing the number of flexible splitters

from one to two, the average power increases from $0.34 \mu W$ to $0.90 \mu W$ at $S^* = 2.5$. The inclusion of the arc plates further improves the harvested power to a maximum value of $3.13 \mu W$.

Consequently, with the perspective of more drag reduction and power generation, placement of piezoelectric polymers would be more effective using CAP with dual flexible splitter plates at $S^* = P^* = 2.5$.

According to the approach of world energy projects and the leap towards clean energy, the use of CAP with flexible splitters, due to the benefits such as easy installation and simplicity, can be helpful in wind energy industries, considering the wind as a huge renewable energy source. High output electrical power of the novel proposed passive control method, at low Reynolds numbers, considerably improves wind energy harvesting applications.

Funding

This research did not receive any specific grant from funding agencies in the public, commercial, or not-for-profit sectors.

CRediT authorship contribution statement

Faezeh Eydi: Writing – original draft, Visualization, Validation, Software, Methodology, Investigation, Formal analysis, Data curation, Conceptualization. **Afsaneh Mojra:** Writing – review & editing, Visualization, Supervision, Project administration, Conceptualization. **Hoo-man Kamel:** Writing – review & editing, Supervision.

Declaration of competing interest

The authors declare that they have no known competing financial interests or personal relationships that could have appeared to influence the work reported in this paper.

References

- Abdelkefi, A., 2016. Aeroelastic energy harvesting: a review. *Int. J. Eng. Sci.* 100, 112–135.
- Abdi, R., Rezazadeh, N., Abdi, M., 2017. Reduction of fluid forces and vortex shedding frequency of a circular cylinder using rigid splitter plates. *European Journal of Computational Mechanics* 26 (3), 225–244.
- Abdi, R., Rezazadeh, N., Abdi, M., 2019. Investigation of passive oscillations of flexible splitter plates attached to a circular cylinder. *J. Fluid Struct.* 84, 302–317.
- Amini, Y., Zahed, I., 2024. Effects of attached flexible splitter plates on flow-induced vibration of two tandem circular cylinders: two-degree of freedoms study. *Ocean. Eng.* 296, 116762.
- Asok, V., Kumar, R.P., Akbar, M.A., 2024. Energy extraction and optimization studies on vortex-induced vibration of the elastically mounted rigid cylinder using wake oscillator model. *Ocean. Eng.* 300, 117515.
- Assi, G., Orselli, R., Silva-Ortega, M., 2019. Control of vortex shedding from a circular cylinder surrounded by eight rotating wake-control cylinders at $Re = 100$. *J. Fluid Struct.* 89, 13–24.

- Averweg, S., Schwarz, A., Schwarz, C., Schröder, J., 2024. A monolithic fluid–structure interaction approach using mixed LSFEM with high-order time integration. *Comput. Methods Appl. Mech. Eng.* 423, 116783.
- Bao, Y., Tao, J., 2013. The passive control of wake flow behind a circular cylinder by parallel dual plates. *J. Fluid Struct.* 37, 201–219.
- Bao, Z., Qin, G., He, W., Wang, Y., 2018. Numerical investigation of flow around a slotted circular cylinder at low Reynolds number. *J. Wind Eng. Ind. Aerod.* 183, 273–282.
- Barrero-Gil, A., Alonso, G., Sanz-Andres, A., 2010. Energy harvesting from transverse galloping. *J. Sound Vib.* 329 (14), 2873–2883.
- Benedetti, I., Gulizzi, V., Milazzo, A., 2019. A microstructural model for homogenisation and cracking of piezoelectric polycrystals. *Comput. Methods Appl. Mech. Eng.* 357, 112595.
- Binyet, E.M., Chang, J.-Y., Huang, C.-Y., 2020. Flexible plate in the wake of a square cylinder for piezoelectric energy harvesting—parametric study using fluid–structure interaction modeling. *Energies* 13 (10), 2645.
- Caracoglia, L., 2018. Modeling the coupled electro-mechanical response of a torsional-flutter-based wind harvester with a focus on energy efficiency examination. *J. Wind Eng. Ind. Aerod.* 174, 437–450.
- Chauhan, M.K., Dutta, S., Gandhi, B.K., 2019. Wake flow modification behind a square cylinder using control rods. *J. Wind Eng. Ind. Aerod.* 184, 342–361.
- Chehreh, B.B., Javadi, K., 2018. Flow control around a circular cylinder with swinging thin plates. *J. Fluid Struct.* 81, 738–760.
- Curatolo, M., La Rosa, M., Prestininzi, P., **Energy Harvesting in a Fluid Flow Using Piezoelectric Materials.**
- Derakhshandeh, J.F., Gharib, N., 2021. Numerical investigations on the flow control over bumped surface circular cylinders. *Ocean. Eng.* 240, 109943.
- Díaz-Ojeda, H., González, L., Huera-Huarte, F., 2019. On the influence of the free surface on a stationary circular cylinder with a flexible splitter plate in laminar regime. *J. Fluid Struct.* 87, 102–123.
- Ding, L., Zhang, L., Bernitsas, M.M., Chang, C.-C., 2016. Numerical simulation and experimental validation for energy harvesting of single-cylinder VIVACE converter with passive turbulence control. *Renew. Energy* 85, 1246–1259.
- Ding, L., Zhang, L., Wu, C., Mao, X., Jiang, D., 2015. Flow induced motion and energy harvesting of bluff bodies with different cross sections. *Energy Convers. Manag.* 91, 416–426.
- Donea, J., Huerta, A., Ponthot, J.P., Rodríguez-Ferran, A., 2004. Arbitrary L agrangian–E ulerian Methods. *Encyclopedia of Computational Mechanics.*
- Duranay, A., 2024. Numerical and experimental investigation of vortex formation modes on a freely vibrating circular cylinder at high Reynolds numbers. *Appl. Ocean Res.* 144, 103909.
- Durhasan, T., 2020. Flow topology downstream of the hollow square cylinder with slots. *Ocean. Eng.* 209, 107518.
- Erturk, A., Inman, D.J., 2011. *Piezoelectric Energy Harvesting.* John Wiley & Sons.
- Eydi, F., Mojra, A., 2023. A numerical study on the benefits of passive-arc plates on drag and noise reductions of a cylinder in turbulent flow. *Phys. Fluids* 35 (8).
- Eydi, F., Mojra, A., Abdi, R., 2022. Comparative analysis of the flow control over a circular cylinder with detached flexible and rigid splitter plates. *Phys. Fluids* 34, 113604.
- Hu, G., Tse, K.T., Wei, M., Naseer, R., Abdelkefi, A., Kwok, K.C., 2018. Experimental investigation on the efficiency of circular cylinder-based wind energy harvester with different rod-shaped attachments. *Appl. Energy* 226, 682–689.
- Hwang, J.-Y., Yang, K.-S., 2007. Drag reduction on a circular cylinder using dual detached splitter plates. *J. Wind Eng. Ind. Aerod.* 95 (7), 551–564.
- Jiang, D., Zhang, H., Yao, W., Zhao, Z., Gui, M., Chen, Z., 2022. The control mechanisms of electromagnetic force for turbulent channel flow with sinusoidal wall deformation. *Ocean. Eng.* 260, 112069.
- Kan, J., Liao, W., Wang, J., Wang, S., Yan, M., Jiang, Y., Zhang, Z., 2021. Enhanced piezoelectric wind-induced vibration energy harvester via the interplay between cylindrical shell and diamond-shaped baffle. *Nano Energy* 89, 106466.
- Karimi-Zindashti, G., Kurç, Ö., 2024. Flow past rotating cylinders using deterministic vortex method. *Ocean. Eng.* 291, 116342.
- Knupp, P.M., 1999. Winslow smoothing on two-dimensional unstructured meshes. *Eng. Comput.* 15 (3), 263–268.
- Kwon, K., Choi, H., 1996. Control of laminar vortex shedding behind a circular cylinder using splitter plates. *Phys. Fluids* 8 (2), 479–486.
- Lai, Z., Wang, S., Zhu, L., Zhang, G., Wang, J., Yang, K., Yurchenko, D., 2021. A hybrid piezo-dielectric wind energy harvester for high-performance vortex-induced vibration energy harvesting. *Mech. Syst. Signal Process.* 150, 107212.
- Liu, F.-R., Zhang, W.-M., Zhao, L.-C., Zou, H.-X., Tan, T., Peng, Z.-K., Meng, G., 2020. Performance enhancement of wind energy harvester utilizing wake flow induced by double upstream flat-plates. *Appl. Energy* 257, 114034.
- Liu, X., Xu, F., Hou, Y., Duan, Z., Ou, J., 2024. Numerical study on passive-jet flow control for chamfered square cylinder. *Ocean. Eng.* 295, 116860.
- Mansy, H., Yang, P.-M., Williams, D.R., 1994. Quantitative measurements of three-dimensional structures in the wake of a circular cylinder. *J. Fluid Mech.* 270 (1), 277–296.
- Mashhadi, A., Sohankar, A., Alam, M.M., 2021. Flow over rectangular cylinder: effects of cylinder aspect ratio and Reynolds number. *Int. J. Mech. Sci.* 195, 106264.
- Mishra, A., Hanzla, M., De, A., 2020. Passive control of the onset of vortex shedding in flow past a circular cylinder using slit. *Phys. Fluids* 32 (1), 013602.
- Monteleone, A., Borino, G., Napoli, E., Burriesci, G., 2022. Fluid–structure interaction approach with smoothed particle hydrodynamics and particle–spring systems. *Comput. Methods Appl. Mech. Eng.* 392, 114728.
- Moradi, M.A., Mojra, A., 2024a. Flow and noise control of a cylinder using grooves filled with porous material. *Phys. Fluids* 36 (4).
- Moradi, M.A., Mojra, A., 2024b. Free-surface flow past a circular cylinder at high Froude numbers. *Ocean. Eng.* 295, 116804.
- Moreno, L., Castañar, I., Codina, R., Baiges, J., Cattoni, D., 2023. Numerical simulation of Fluid–Structure Interaction problems with viscoelastic fluids using a log-conformation reformulation. *Comput. Methods Appl. Mech. Eng.* 410, 115986.
- Murali, D., Petha Sethuraman, V.R., 2024. Flow control using hot splitter plates in the wake of a circular cylinder: a hybrid strategy. *Phys. Fluids* 36 (1).
- Nam, S.H., Yoon, H.S., 2022. Effect of the wavy geometric disturbance on the flow over elliptic cylinders with different aspect ratios. *Ocean. Eng.* 243, 110287.
- Naseer, R., Dai, H., Abdelkefi, A., Wang, L., 2017. Piezomagnetoelastic energy harvesting from vortex-induced vibrations using monostable characteristics. *Appl. Energy* 203, 142–153.
- Norberg, C., 2003. Fluctuating lift on a circular cylinder: review and new measurements. *J. Fluid Struct.* 17 (1), 57–96.
- Ozkan, G.M., Firat, E., Akilli, H., 2017. Passive flow control in the near wake of a circular cylinder using attached permeable and inclined short plates. *Ocean. Eng.* 134, 35–49.
- Priya, S., Inman, D.J., 2009. *Energy Harvesting Technologies.* Springer.
- Qin, W., Deng, W., Pan, J., Zhou, Z., Du, W., Zhu, P., 2019. Harvesting wind energy with bi-stable snap-through excited by vortex-induced vibration and galloping. *Energy* 189, 116237.
- Ramadan, K.S., Sameoto, D., Evoy, S., 2014. A review of piezoelectric polymers as functional materials for electromechanical transducers. *Smart Mater. Struct.* 23 (3), 033001.
- Rastan, M., Sohankar, A., Doolan, C., Moreau, D., Shirani, E., Alam, M.M., 2019. Controlled flow over a finite square cylinder using suction and blowing. *Int. J. Mech. Sci.* 156, 410–434.
- Rezaei, M., Talebitooti, R., Liao, W.-H., 2022. Investigations on magnetic bistable PZT-based absorber for concurrent energy harvesting and vibration mitigation: numerical and analytical approaches. *Energy* 239, 122376.
- Richter, T., Wick, T., 2010. Finite elements for fluid–structure interaction in ALE and fully Eulerian coordinates. *Comput. Methods Appl. Mech. Eng.* 199 (41–44), 2633–2642.
- Sharma, B., Barman, R., 2020. Steady laminar flow past a slotted circular cylinder. *Phys. Fluids* 32 (7), 073605.
- Sharma, K., Dutta, S., 2020. Flow control over a square cylinder using attached rigid and flexible splitter plate at intermediate flow regime. *Phys. Fluids* 32 (1), 014104.
- Song, J., Hu, G., Tse, K., Li, S., Kwok, K., 2017. Performance of a circular cylinder piezoelectric wind energy harvester fitted with a splitter plate. *Appl. Phys. Lett.* 111 (22), 223903.
- Stamatellou, A.-M., Kalfas, A.I., 2019. Testing of piezoelectric energy harvesters isolated from base vibrations. *Energy Convers. Manag.* 196, 717–728.
- Su, W.-J., Lin, W.-Y., 2020. Design and analysis of a vortex-induced bi-directional piezoelectric energy harvester. *Int. J. Mech. Sci.* 173, 105457.
- Sudhakar, Y., Vengadesan, S., 2012. Vortex shedding characteristics of a circular cylinder with an oscillating wake splitter plate. *Comput. Fluids* 53, 40–52.
- Sun, W., Jo, S., Seok, J., 2019. Development of the optimal bluff body for wind energy harvesting using the synergetic effect of coupled vortex induced vibration and galloping phenomena. *Int. J. Mech. Sci.* 156, 435–445.
- Sun, X., Suh, C.S., Sun, C., Yu, B., 2021. Vortex-induced vibration of a flexible splitter plate attached to a square cylinder in laminar flow. *J. Fluid Struct.* 101, 103206.
- Taheri, E., Zhao, M., Wu, H., Munir, A., 2021. Energy harvesting from inline vibration of an elastically mounted circular cylinder in oscillatory flow. *Ocean. Eng.* 239, 109694.
- Turek, S., Hron, J., 2006. *Proposal for Numerical Benchmarking of Fluid-Structure Interaction between an Elastic Object and Laminar Incompressible Flow, Fluid-Structure Interaction.* Springer, pp. 371–385.
- Wang, C., Tang, H., Duan, F., Simon, C., 2016. Control of wakes and vortex-induced vibrations of a single circular cylinder using synthetic jets. *J. Fluid Struct.* 60, 160–179.
- Wang, J., Zhang, C., Zhang, M., Abdelkefi, A., Yu, H., Ge, X., Liu, H., 2021a. Enhancing energy harvesting from flow-induced vibrations of a circular cylinder using a downstream rectangular plate: an experimental study. *Int. J. Mech. Sci.* 211, 106781.
- Wang, J., Zhou, S., Zhang, Z., Yurchenko, D., 2019. High-performance piezoelectric wind energy harvester with Y-shaped attachments. *Energy Convers. Manag.* 181, 645–652.
- Wang, S., Liao, W., Zhang, Z., Liao, Y., Yan, M., Kan, J., 2021b. Development of a novel non-contact piezoelectric wind energy harvester excited by vortex-induced vibration. *Energy Convers. Manag.* 235, 113980.
- Williamson, C.H., 1989. Oblique and parallel modes of vortex shedding in the wake of a circular cylinder at low Reynolds numbers. *J. Fluid Mech.* 206, 579–627.
- Xiong, H., Wang, L., 2016. Piezoelectric energy harvester for public roadway: on-site installation and evaluation. *Appl. Energy* 174, 101–107.
- Xu, W., Zhang, S., Ma, Y., Liu, B., Wang, J., 2021. A study on the FIV hydrodynamic force coefficients of two staggered flexible cylinders via an inverse method. *Ocean. Eng.* 219, 108272.
- Xue, Z., Han, B., Zhang, H., Xin, D., Zhan, J., Wang, R., 2021. External suction-blowing method for controlling vortex-induced vibration of a bridge. *J. Wind Eng. Ind. Aerod.* 215, 104661.
- Yang, Q., Liu, Z., Hui, Y., Li, Z., 2020. Modification of aerodynamic force characteristics on high-rise buildings with arrangement of vertical plates. *J. Wind Eng. Ind. Aerod.* 200, 104155.
- Yu, H., Zhang, M., 2021. Effects of side ratio on energy harvesting from transverse galloping of a rectangular cylinder. *Energy* 226, 120420.

- Yu, K., Qu, B., Yue, C., Ge, S., Chen, X., Liang, J., 2019. A performance-guided JAYA algorithm for parameters identification of photovoltaic cell and module. *Appl. Energy* 237, 241–257.
- Zhang, M., Xu, F., Han, Y., 2020. Assessment of wind-induced nonlinear post-critical performance of bridge decks. *J. Wind Eng. Ind. Aerod.* 203, 104251.
- Zhang, M., Zhang, C., Abdelkefi, A., Yu, H., Gaidai, O., Qin, X., Zhu, H., Wang, J., 2021. Piezoelectric energy harvesting from vortex-induced vibration of a circular cylinder: effect of Reynolds number. *Ocean. Eng.* 235, 109378.
- Zhao, L.-C., Zou, H.-X., Yan, G., Liu, F.-R., Tan, T., Zhang, W.-M., Peng, Z.-K., Meng, G., 2019. A water-proof magnetically coupled piezoelectric-electromagnetic hybrid wind energy harvester. *Appl. Energy* 239, 735–746.
- Zhu, H., Li, G., Wang, J., 2020. Flow-induced vibration of a circular cylinder with splitter plates placed upstream and downstream individually and simultaneously. *Appl. Ocean Res.* 97, 102084.
- Zhu, H., Liao, Z., Gao, Y., Zhao, Y., 2017. Numerical evaluation of the suppression effect of a free-to-rotate triangular fairing on the vortex-induced vibration of a circular cylinder. *Appl. Math. Model.* 52, 709–730.
- Zhu, H., Liu, W., 2020. Flow control and vibration response of a circular cylinder attached with a wavy plate. *Ocean. Eng.* 212, 107537.
- Zhu, H., Zhou, T., 2019. Flow around a circular cylinder attached with a pair of fin-shaped strips. *Ocean. Eng.* 190, 106484.